



HAL
open science

Cenozoic volcanism in the Bohemian Massif in the context of P- and S-velocity high-resolution teleseismic tomography of the upper mantle

Jaroslava Plomerová, Helena Munzarová, Luděk Vecsey, Eduard Kissling, Ulrich Achauer, Vladislav Babuška

► To cite this version:

Jaroslava Plomerová, Helena Munzarová, Luděk Vecsey, Eduard Kissling, Ulrich Achauer, et al.. Cenozoic volcanism in the Bohemian Massif in the context of P- and S-velocity high-resolution teleseismic tomography of the upper mantle. *Geochemistry, Geophysics, Geosystems*, 2016, 17 (8), pp.3326-3349. 10.1002/2016GC006318 . hal-03514613

HAL Id: hal-03514613

<https://cnrs.hal.science/hal-03514613v1>

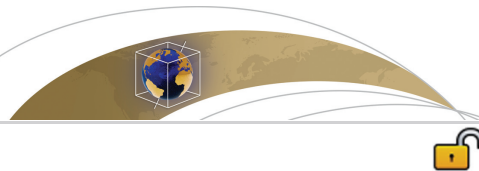
Submitted on 6 Jan 2022

HAL is a multi-disciplinary open access archive for the deposit and dissemination of scientific research documents, whether they are published or not. The documents may come from teaching and research institutions in France or abroad, or from public or private research centers.

L'archive ouverte pluridisciplinaire **HAL**, est destinée au dépôt et à la diffusion de documents scientifiques de niveau recherche, publiés ou non, émanant des établissements d'enseignement et de recherche français ou étrangers, des laboratoires publics ou privés.



Distributed under a Creative Commons Attribution - NonCommercial - ShareAlike 4.0 International License



RESEARCH ARTICLE

10.1002/2016GC006318

Key Points:

- Velocity-perturbation patterns in the P- and S-wave models exhibit similar features
- None of the models display a clear narrow “plume-like” structure
- Broad shape of heterogeneity and no evident connection with deeper parts support interpretation by lithosphere thinning along Eger Rift

Supporting Information:

- Supporting Information S1

Correspondence to:

J. Plomerová,
jpl@ig.cas.cz

Citation:

Plomerová, J., H. Munzarová, L. Vecsey, E. Kissling, U. Achauer, and V. Babuška (2016), Cenozoic volcanism in the Bohemian Massif in the context of P- and S-velocity high-resolution teleseismic tomography of the upper mantle, *Geochem. Geophys. Geosyst.*, 17, 3326–3349, doi:10.1002/2016GC006318.

Received 23 FEB 2016

Accepted 22 JUL 2016

Accepted article online 2 AUG 2016

Published online 19 AUG 2016

The copyright line for this article was changed on 12 OCT 2016 after original online publication.

© 2016. The Authors.

This is an open access article under the terms of the Creative Commons Attribution-NonCommercial-NoDerivs License, which permits use and distribution in any medium, provided the original work is properly cited, the use is non-commercial and no modifications or adaptations are made.

Cenozoic volcanism in the Bohemian Massif in the context of P- and S-velocity high-resolution teleseismic tomography of the upper mantle

Jaroslava Plomerová¹, Helena Munzarová¹, Luděk Vecsey¹, Eduard Kissling², Ulrich Achauer³, and Vladislav Babuška¹

¹Institute of Geophysics, Academy of Sciences of the Czech Republic, Prague, Czech Republic, ²Institute of Geophysics, Swiss Federal Institute of Technology, Zürich, Switzerland, ³Institute of Earth Physics, University of Strasbourg, Strasbourg, France

Abstract New high-resolution tomographic models of P- and S-wave isotropic-velocity perturbations for the Bohemian upper mantle are estimated from carefully preprocessed travel-time residuals of teleseismic P, PKP and S waves recorded during the BOHEMA passive seismic experiment. The new data resolve anomalies with scale lengths 30–50 km. The models address whether a small mantle plume in the western Bohemian Massif is responsible for this geodynamically active region in central Europe, as expressed in recurrent earthquake swarms. Velocity-perturbations of the P- and S-wave models show similar features, though their resolutions are different. No model resolves a narrow subvertical low-velocity anomaly, which would validate the “baby-plume” concept. The new tomographic inferences complement previous studies of the upper mantle beneath the Bohemian Massif, in a broader context of the European Cenozoic Rift System (ECRIS) and of other Variscan Massifs in Europe. The low-velocity perturbations beneath the Eger Rift, observed in about 200km-broad zone, agree with shear-velocity models from full-waveform inversion, which also did not identify a mantle plume beneath the ECRIS. Boundaries between mantle domains of three tectonic units that comprise the region, determined from studies of seismic anisotropy, represent weak zones in the otherwise rigid continental mantle lithosphere. In the past, such zones could have channeled upwelling of hot mantle material, which on its way could have modified the mantle domain boundaries and locally thinned the lithosphere.

1. Introduction

The western Bohemian Massif belongs to one of the most geodynamically active regions in central Europe. The BOHEMA passive seismic experiment [Plomerová *et al.*, 2003] was designed to confirm or to reject the existence of a small mantle plume as a possible cause of this activity and the Cenozoic volcanism. Tomography of the upper mantle is a powerful tool to image structures of Earth's interior. Velocity perturbations to a simple background model provide essential information on the deep structures. The upper mantle beneath the Bohemian Massif (BM) appears as a part of an extensive low-velocity region beneath central Europe detected in various large-scale tomographic studies of Europe [e.g., Goes *et al.*, 1999; Wortel and Spakman, 2000; Piromallo and Morelli, 2003; Amaru, 2007; Koulakov *et al.*, 2009]. However, the resolution of such tomographic images, based on travel times of body waves measured at permanent observatories in the area, is not sufficient to infer upper-mantle structures at scales less than ~100 km.

Temporary arrays of seismic stations, which were deployed in Europe during the last two decades (e.g., Eifel [Ritter *et al.*, 2001]; SVEKALAPKO [Sandoval *et al.*, 2004]; TransAlp [Lippitsch *et al.*, 2003; Kissling *et al.*, 2006]; CALIXTO [Weidle *et al.*, 2005]; TOR [Shomali *et al.*, 2006]; BOHEMA [Plomerová *et al.*, 2007]; PASSEQ [Wilde-Piórko *et al.*, 2008]; TOPOIBERIA [Díaz *et al.*, 2015]), recorded data for a more-detailed regional research, as well as for a comprehensive model beneath all Europe, down to the lower mantle [Amaru, 2007]. Two recent teleseismic tomography studies based on body waves recorded by temporary arrays in the Carpathians-Pannonian region (Carpathian Basin Project) [Dando *et al.*, 2011] and the Eastern Alps (ALPASS) [Mitterbauer *et al.*, 2011] presented detailed velocity models of the upper mantle south-eastward and southward of the BM, respectively, but improved only marginally the resolution of the BM, due to the large spacing of the permanent observatories and low resolution at the spatial boundaries of the models.

Our long-term research of the BM upper-mantle structure has been based on data from several temporary arrays, which step-by-step covered the massif (MOSAIC, BOHEMA I-III) [Plomerová *et al.*, 2005, 2007, 2012; Babuška *et al.*, 2008; Karousová *et al.*, 2012b, 2013]. In these deployments we focused both on isotropic P velocity in the upper mantle and on detecting seismic velocity anisotropy. The research resulted in 3D models of the mantle lithosphere fabrics consistent with mapped boundaries of the lithospheric domains, as well as estimates of the lithosphere-asthenosphere boundary by different methods [Plomerová *et al.*, 2012; Geissler *et al.*, 2012; Babuška and Plomerová, 2013].

The Bohemian Massif is the largest of the Variscan Massifs with one of the smallest rifts of the European Cenozoic Rift System (ECRIS) and the most wide-spread Cenozoic volcanism within the massif. Granet *et al.* [1995] hypothesized that there are several “baby-plumes,” that is, narrow subvertical low-velocity anomalies in the European upper mantle, associated with regions of the Tertiary-Quaternary volcanism. The low-velocity material feeding the “baby plumes” was commonly assumed to lie deeper in the mantle. According to the “baby plume” hypothesis, such low-velocity anomalies are suggested in the mantle beneath five regions of the ECRIS, namely the French Massif Central, Rhenish Massif, Rhine Graben, Bohemian Massif and the Pannonian Basin. However, such tube-like low-velocity anomalies have been imaged in teleseismic P-wave tomography only beneath the first two of the five, i.e., beneath the French Massif Central (MC) [Granet *et al.*, 1995] and the Rhenish Massif (RM) [Ritter *et al.*, 2001]. The RM anomaly was also interpreted to cause variations in the shear-wave splitting above the Eifel hotspot [Walker *et al.*, 2005]. However, up to now, no baby plume has been found beneath other rifts of the ECRIS, such as beneath the Rhine Graben in the Vosges-Black Forest region [Achauer and Masson, 2002], or, in preliminary P-wave tomography beneath the Eger Rift in the western BM [Plomerová *et al.*, 2007]. Similarly, no “baby plume” was identified in the tomographic models beneath the Pannonian Basin [Chang *et al.*, 2010; Dando *et al.*, 2011], a region with extensive Cenozoic volcanism, comparable with that of the MC.

This paper aims at presenting the most detailed images of P- and S-velocity perturbations to date of the western BM upper mantle down to ~350 km. In this region, where the existence of one of the “baby plume” structures was suggested, a temporary regional network of densely spaced stations was installed within the framework of the Czech-French-German project BOHEMA [Plomerová *et al.*, 2003]. Our high-resolution P-velocity perturbation model is computed from a new set of carefully picked PKP arrival times combined with an extended set of previously processed P-wave data that provided the first insight into the upper-mantle velocities [Plomerová *et al.*, 2007]. The new extended data set underwent independent preprocessing compared to the previous study. We used a new update of the inversion code [Karousová *et al.*, 2013] with different model parameterization. Moreover, *a priori* crustal corrections were used to minimize the leakage of crustal velocity perturbations into the upper-mantle images [Karousová *et al.*, 2012a]. To get independent information, we measured also S-wave arrivals, because S waves are even more sensitive to a potential velocity decrease due to an increase of temperature or a decrease of viscosity in the upper-mantle material. To minimize potential effects of inclined anisotropic structures in the mantle lithosphere domains on isotropic tomographic images [e.g., Babuška and Plomerová, 2013, and references therein], we measure separately S-arrivals on the T (transverse) and the Q (perpendicular to T in the ray plane) components, without any intention to judge an anisotropic structure of the upper mantle from standard isotropic tomography. The new tomographic images have the highest resolution in the western part of the BM, where a hypothetical “baby-plume” was anticipated in analogy with the concept of Granet *et al.* [1995]. Tomographic studies combining independent data sets could shed new light on architecture of the upper mantle also in other regions where small-size plumes were suggested.

2. Tectonic Background

2.1. Variscan Massifs and ECRIS

Variscan massifs in Phanerozoic Europe vary in size, amount and extent of rifts and the Cenozoic volcanism (Figure 1). The Bohemian Massif (BM) represents the easternmost and the most prominent relic of the Late Paleozoic collisional belt of the Variscides in central Europe [Franke, 2006; Linnemann *et al.*, 2008]. The BM unit assemblage was created during the Variscan cycle resulting from the collision of two major continents—Gondwana to the south and Laurentia-Baltica to the north [Matte, 1986]. Between these two continents, small microplates, separated by ocean basins, drifted during the early Paleozoic. Some of them collided to

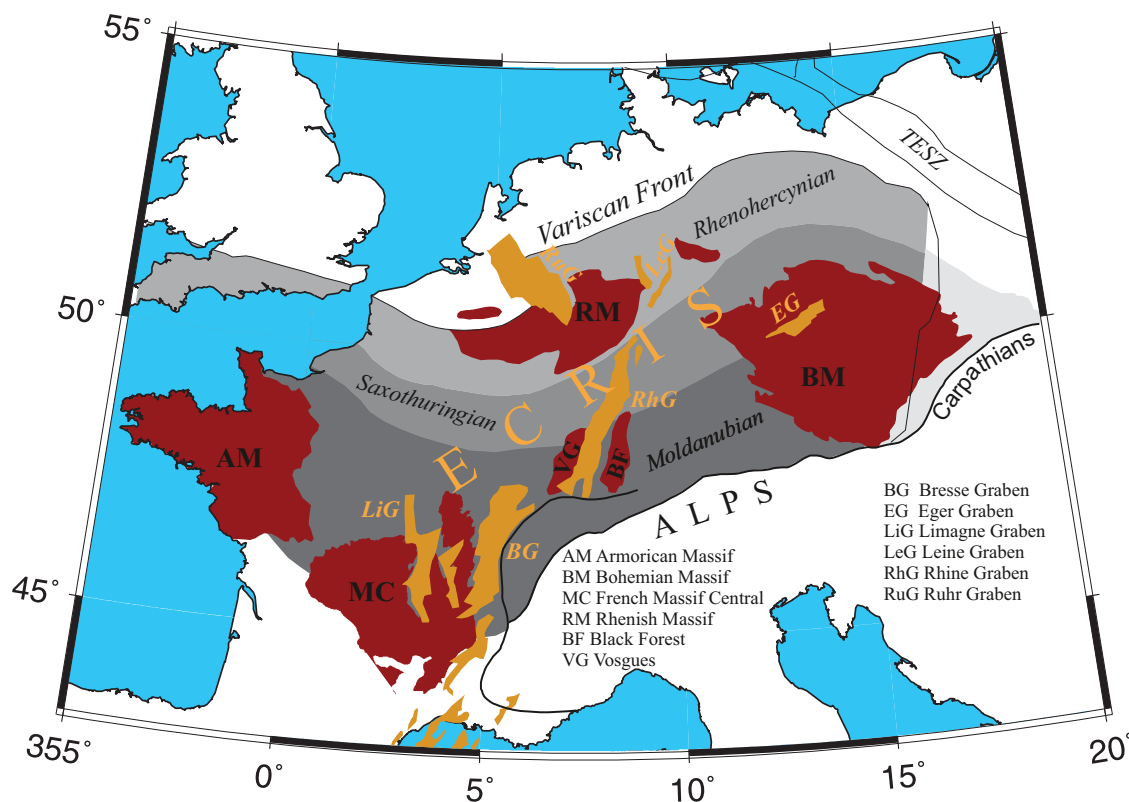


Figure 1. Variscan orogenic belt, massifs and European Cenozoic Rift System (ECRIS).

form the BM from the Silurian to the Permian. In the Mesozoic and Cenozoic eras, the BM formed the northern foreland of the Alpine orogen. Stresses within the European lithosphere caused by the Atlantic opening and the Alpine orogeny resulted in rifting and alkaline volcanism in central and western Europe [e.g., Ziegler and Dezes, 2006; Ziegler et al., 2006].

The European Cenozoic Rift System (ECRIS) [Ziegler, 1992] extends from the Dutch North Sea coast southward to the Western Mediterranean and spans from western Europe far into its central/eastern part (Figure 1). Graben structures of the rift system are linked through transfer zones or transform fault systems. The Tertiary Eger (Ohře) Rift (ER) is an ENE-WSW striking structure, exhibiting a slightly enhanced heat flow [Čermák, 1994] and wide-spread Cenozoic volcanism [Ulrych et al., 2000]. The rift structure developed in the western part of the BM, where three major tectonic units - the Saxothuringian (ST) in the north and the Teplá-Barrandian (TB) and the Moldanubian (MD) units in the south have converged (Figure 2a). The distinct ~120 km long graben structure in the ER developed above the steep ST-TB mantle-lithosphere boundary. From the large extent of volcanism we can assume the rift structure (ER) continues in the mantle lithosphere to the southwest and to the northeast on both ends of the Eger Graben (EG), i.e., beyond the Mariánské-Lázně Fault (MLF) and Elbe Fault Zone (EFZ) zones that limit the graben (EG; Figure 2).

The ER represents an integral part of the European Cenozoic Rift System, which evolved in response to passive rifting related to compressional stresses during the Alpine and Pyrenean collisions [Ziegler, 1992; Dezes et al., 2004]. Though mantle-plume activity is not considered to drive the rifting, evolution of the ECRIS was accompanied by the development of major volcanic centers in the French Massif Central and in the Rhenish and Bohemian Massifs [Ziegler and Dezes, 2006]. This led to the hypothesis, supported by results of seismic tomography [Goes et al., 1999; Ritter et al., 2001; Amaru, 2007], that the ECRIS may have a common source of "plume-like" volcanism in the mantle, manifested by "baby-plumes" beneath the Variscan massifs [Granet et al., 1995; Ritter et al., 2001].

From the geodynamical point of view, the western BM is the most active part of the massif. Recent tectonic activity is primarily associated with Cenozoic volcanism [Ulrych et al., 2000], gas emanations containing high

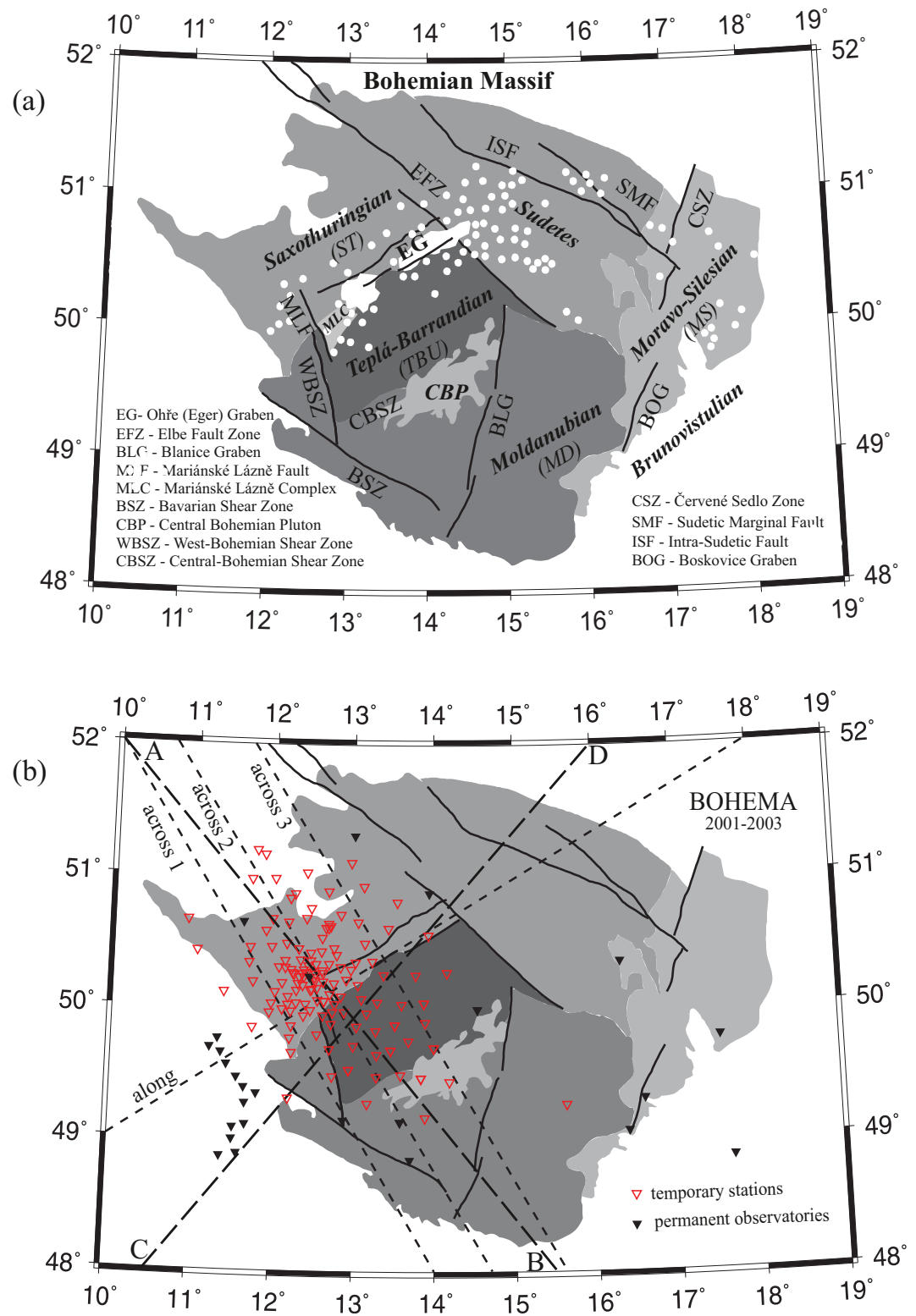


Figure 2. Simplified tectonic map of the Bohemian Massif showing (a) major units, faults and volcanism (white), and (b) seismic stations of the BOHEMA passive experiment. Dashed lines locate the cross sections through tomography images of velocity perturbations presented in Figures 8 and 10; supporting information Figure S5.

proportions of mantle-derived CO₂ and ³He [Kämpf *et al.*, 2013], as well as by episodic shallow earthquake swarms [Horálek and Fischer, 2008] and neotectonic crustal movements [Bankwitz *et al.*, 2003; Peterek *et al.*, 2011]. The question of a possible source of mantle fluids is important, namely in relation to the increase of ³He/⁴He ratios observed by Bräuer *et al.* [2005]. The authors interpret primitive helium as evidence for ascending mantle-derived melt and as an indication of a possible volcanic activity.

2.2. BM Crust and Lithosphere-Asthenosphere Boundary

The structure of the western-BM lower lithosphere and the depth of the lithosphere-asthenosphere boundary (LAB) have been subjects of several studies since the early 80s [e.g., Babuška *et al.*, 1987]. The lithosphere thins to 80–90 km along the ER [Plomerová *et al.*, 1998] in models which exploit the increased velocity contrast across the LAB, caused by orientation differences in seismic anisotropy within the lower lithosphere and the sublithosphere mantle [e.g., Plomerová and Babuška, 2010]. Lithosphere thinning up to about 65 km has been identified by the *S*-receiver function method [Heuer *et al.*, 2007] in the western part of the ER. Preliminary results of the teleseismic P-wave travel-time tomography down to a depth of about 270 km by Plomerová *et al.* [2007] did not recognize any “tube-like” low-velocity anomaly which could be interpreted as a mantle plume beneath the western part of the ER.

The average thickness of the BM crust is about 33 km, but Moho depth varies between 26 and 40 km on relatively short distances. The crust is thinner around the junction of the Saxothuringian/Teplá Barradian/Moldanubian tectonic units in the western part of the massif. According to the refraction model of Hrubcová *et al.* [2005], the thinnest crust of about 30 km is characteristic for the ST-TB transition. Moreover, the authors identified the top of a highly reflective lower-crustal layer up to 9 km thick at ~26 km depth beneath the ST unit, whereas beneath the TB and MD units the Moho appears as a sharp velocity discontinuity. With the use of the *Ps* receiver functions, Geissler *et al.* [2005] and Heuer *et al.* [2006] interpret Moho depths as shallow as 24 km beneath the junction of the three tectonic units. Differences in the Moho depths modeled by the two methods are 5–6 km in the Saxothuringian, while in the TB unit and further in the Moldanubian, the results of both methods are consistent [Karousová *et al.*, 2012a]. The authors attribute the different Moho depths from the controlled-source seismics and receiver-function method to a much larger sensitivity to the sharpness of the velocity contrast of the latter method. Hrubcová and Geissler [2009] admit that an unclear reflection from the weakly reflective Moho 30–32 km can be masked by a strong reflection from the top of the reflective transition zone at about 28 km and thus can lead to the different Moho depths in the ST. Average P velocities in the west Bohemian crust vary between 6.1 and 6.3 km/s, with the highest values in the Mariánské-Lázně Complex (MLC), an exhumed block of the lower crust [Jelínek *et al.*, 1997]

3. Data

Shear waves are strongly sensitive to a velocity decrease, particularly in the presence of melt or mantle fluids. Therefore, we measured shear-wave arrival times on recordings of the BOHEMA array (Figure 2b) operated during the 2001–2003 to complement results of the preliminary P-wave tomography [Plomerová *et al.*, 2007], which reflected gross features of P-velocity variation without any detailed tectonic correlations.

We have evaluated manually arrival times on the broad-band recordings of direct *S*, core-mantle refracted SKS, SKKS or PKS waves as well as several reflected phases, e.g., *sS*, *ScS*, *SS* of events with magnitudes at least 5 from epicentral distances 30°–145° (Figure 3). To avoid an additional bias into isotropic tomography coming from upper-mantle anisotropic structure beneath the western BM (average shear-wave split-delay time $\delta t = 1.2$ s [Babuška *et al.*, 2008]), we rotated the Z, N, E geographical components of the shear-wave recordings into the L, Q, T ray-parameter coordinate system, in which the L and Q axes lie in the ray planes and L is oriented in the ray direction and, the T axis is perpendicular to the (L,Q) plane. Then we picked the arrival times of shear waves with SH and SV polarizations (denoted here as ST and SQ phases) separately on the T and Q components for 60 and 83 teleseismic events, respectively. The input files for the tomography consist of 1464 and 1943 travel times of ST and SQ shear phases measured at 77 broad-band temporary stations of the BOHEMA array and seismological observatories in the region. The stations were equipped mostly with STS2 and several Guralp CMG-3T, CMG-3ESP and CMG-T40 seismometers, and various data acquisition systems (<http://www.ig.cas.cz/en/structure/observatories/mobile-seismic-stations/map-stations>).

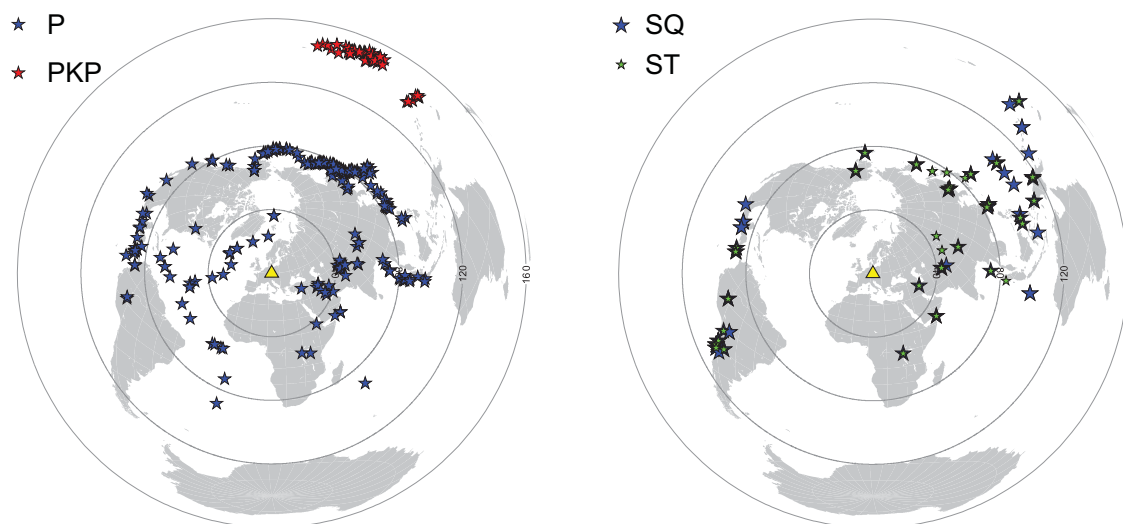


Figure 3. Distribution of earthquake foci from which travel times of P, PKP and shear waves are analyzed.

Dominant periods of shear waves are 6–10 s, i.e., in flat parts of seismic sensor responses, thus without a need to correct for instrument response.

We picked the shear-wave arrival times in a standard way, i.e., by the first clear extremes of the shear waveforms correlated across the array (Figure 4) with the use of Seismic Handler software [Stammler, 1993]. A quality factor of each measurement was set according to the uncertainty of the picking and used in the weighting matrix during the tomography inversion. We recalculated the correlated picks of an event into absolute arrival times according to one or several clear phase onsets of the event. Absolute travel-time residuals were calculated relative to the IASP'91 model [Kennett and Engdahl, 1991] and their time stability of relative residual was tested to avoid any instrumental effects, e.g., due to occasional failures of time synchronization at some of the temporary stations.

To reduce effects of the heterogeneous crust with variable Moho depth and to prevent their mapping into velocity-perturbation images of the upper mantle, the absolute residuals were corrected for differences between the crust velocities of the reference IASP'91 model and the smooth velocity model of the BM crust [Karousová *et al.*, 2012a]. Travel times in the upper crust can be affected locally by thick sediments. Therefore, we applied corrections for sediments, where sedimentary layer was thick enough to slow down the teleseismic P waves by at least 0.1s. Applying the deterministic crustal corrections in a tomographic inversion leads to smoother perturbations at shallow mantle depths (see supporting information Figure S6) compared with those [Plomerová *et al.*, 2007, Figure 2] calculated from travel times corrected by “layer-stripping” approach [Evans and Achauer, 1993].

The same rules were applied in careful estimation of arrival times for different branches of the PKP phases from recordings of 58 earthquakes (Figure 3). The correlated times were picked on Z components of both the short-period and broad-band stations of the BOHEMA array, all corrected for the WWSSN responses. Most of the measurements were of the highest quality, i.e., with measurement accuracy of one sample (± 0.05 s on recordings with 20 Hz sampling). The 3763 PKP travel times augmented a new set of 14013 high-quality P-wave arrivals. The new set of P-wave arrival times includes measurements made for the inversion of Plomerová *et al.* [2007], complemented by P arrivals mostly from the less well-covered SW quadrant.

Tomographic images of the P- and S-velocity perturbations are calculated from relative residuals of both the P+PKP and S waves, respectively. Event residual means were subtracted from measurements at individual stations to suppress heterogeneities out of the region. 98% of 17776 relative residuals in the P+PKP tomography input lie in interval (-1 s, 1 s) out of which 96% are in interval (-0.7 s, 0.7 s), the residual range of the 2007 inversion [Plomerová *et al.*, 2007]. Number of intersecting rays increases in the new input for P-velocity perturbation model, which represents significant improvement for tomography resolution.

02/03/03 12:08:19.7 HINDU KUSH REGION - S wave

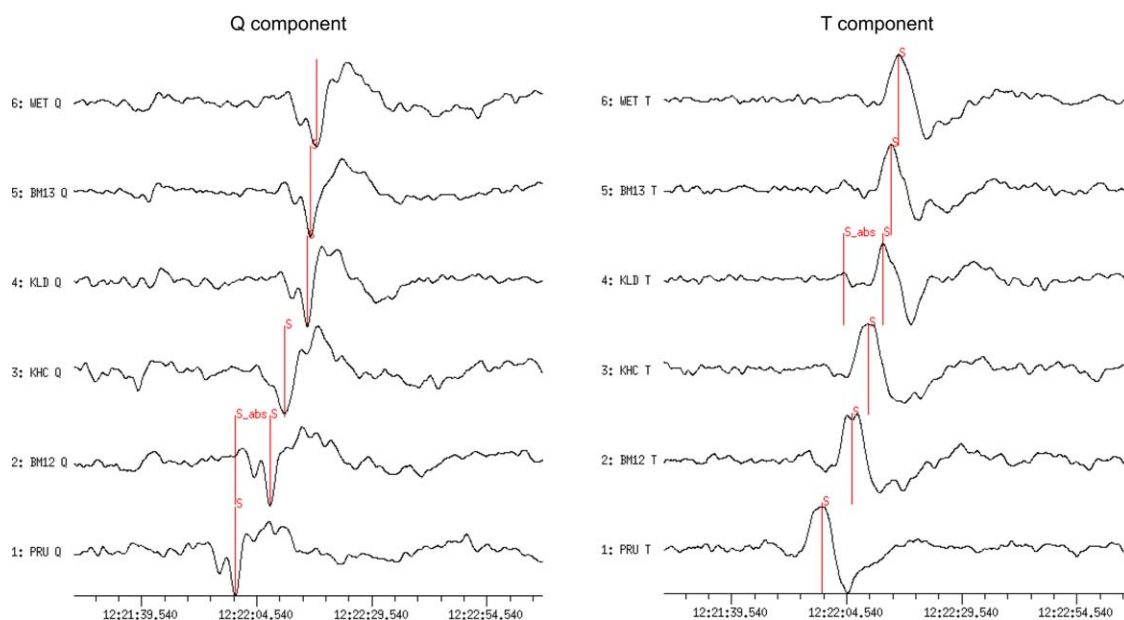


Figure 4. Examples of shear-wave picking on the Q and T components of several stations of the BOHEMA array.

4. Seismic Tomography–Method and Model Parameterization

Teleseismic tomography images spatial distribution and magnitude of velocity perturbations estimated by back-projection of relative travel-time residuals into the target volume, which is, in case of regional tomography, the upper mantle beneath the array of seismic stations. We have updated the frequently used TELINV tomographic code (<http://www.ig.cas.cz/en/research-teaching/software-download/>), which is based on a modified nonlinear inversion scheme known as the ACH method [Aki *et al.*, 1977; Evans and Achauer, 1993]. During the tomography calculation, a starting reference velocity model, in our case the IASP'91 radial Earth model [Kennett and Engdahl, 1991], is iteratively adjusted by solving a system of linearized travel-time equations which relate the relative travel-time residuals Δt to the velocity perturbations Δv^i along the ray path, composed of segments s_i ,

$$\Delta t = \sum_i \left(\frac{\partial t}{\partial v} \right)_i \Delta v^i = \sum_i - \frac{s_i}{v_i^2} \Delta v^i. \quad (1)$$

The task is solved by a weighted damped least-square method [Menke, 1984]

$$m = (A^T W_D A + \varepsilon^2 W_M)^{-1} A^T W_D d \quad (2)$$

where m is vector of unknown velocity perturbations, d is data vector containing travel-time residuals Δt . The partial derivatives in (1) are stored in matrix A . Weighting matrix W_D contains errors of arrival-time measurements. The ill-posed problem is stabilized by damping factor ε^2 and smoothing matrix W_M . The matrix inverse is approximated by truncated singular value decomposition. The 3D ray-tracing bending technique Simplex [Steck and Prothero, 1991], in which ray paths are distorted by sinusoidal signals, is applied. Though the starting model is arbitrary, it should be close to the real velocity distribution, to satisfy the assumption of linearization of the travel-time equations. The velocity perturbations evaluated from relative residuals express velocity variations within each horizontal layer and should not be converted into the absolute velocities.

The velocity perturbations are calculated at nodes of an orthogonal 3D grid, parameterizing velocities of the model volume. Off the nodes, the perturbations are linearly interpolated considering velocities of the surrounding nodes. The grid spacing depends on ray geometry, given by the station-event distribution, and on a dominant wavelength of teleseismic body waves. We chose horizontal grid spacing of 30 km, from the

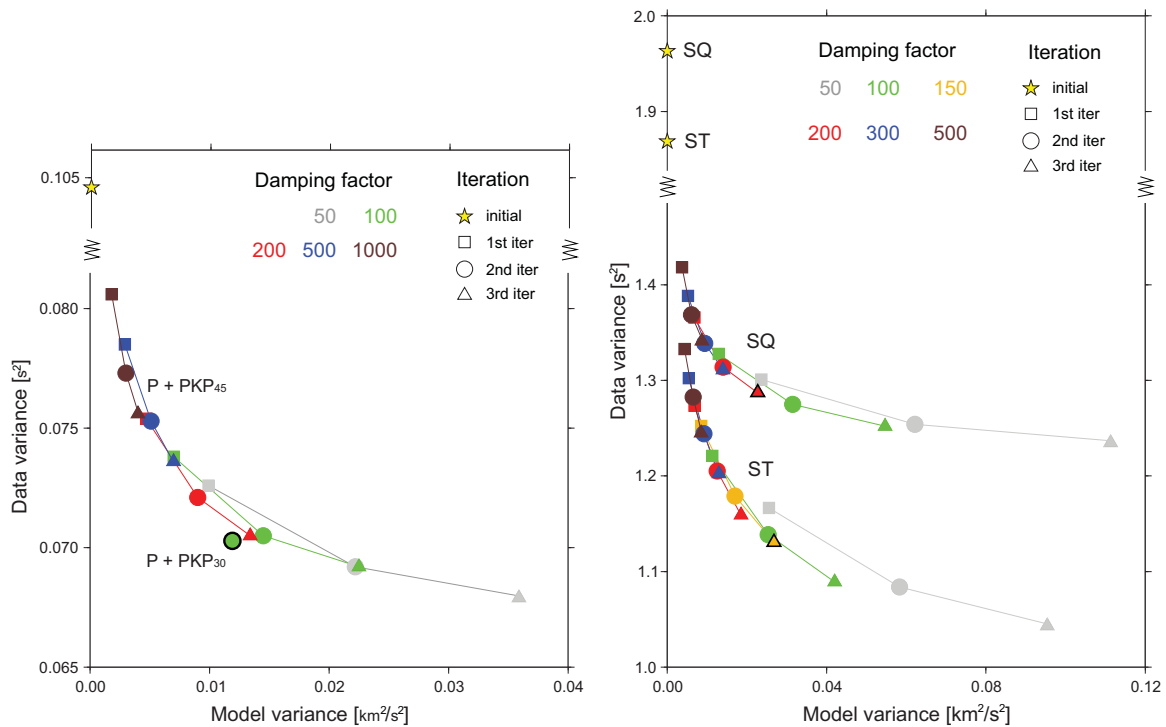


Figure 5. Data and Model variance trade-off curves for different damping factors and number of iterations. The final parameters are black contoured.

30, 45, 60 km tested, as it provided the most stable results for both the P- and S-wave data sets. The selected spacing reflects the relatively small size of individual tectonic units within the BM. Apart from influence of the spacing on the results, we tested the effect of grid position in relation to the known mantle block boundaries [e.g., Babuška and Plomerová, 2013] by shifting the grid in different directions.

The initial vertical spacing of the nodes between depths of 35 km and 350 km was 45 km for both P and S waves. However, the large number of the P and PKP arrivals allowed refinement to 30km starting from 20 km depth (Figure 5). Note that the P+PKP₃₀ model (i.e., the model with the 30km vertical grid spacing calculated from the P and PKP relative residuals) variance is lower than for P+PKP₄₅ (the same but with the 45km vertical grid spacing) at approximately the same data variance level. Total number of inverted nodes was 1144 for two S-velocity perturbation models, and 2176 and 3264 for the P₄₅- and refined P₃₀-velocity perturbation models, respectively. The perturbations at the first inverted depths are resolved less reliably due to the ray steepness and the resulting lack of ray intersections. Perturbations at nodes at crustal levels tend to absorb imperfect crustal corrections and data errors, which would otherwise project into deeper parts of the model.

The damping parameters, smoothing and number of iterations control stability and complexity of the solution [Lippitsch et al., 2003]. We selected these parameters according to the trade-off curves (Figure 5) with a criterion that velocity perturbations must have a physical meaning, i.e., amplitudes of perturbations should be consistent with the velocity range of upper-mantle rocks. Damping parameters of 100, 200 and 150 were selected for P, SQ and ST waves, respectively, by estimating the inflection points of the trade-off curves between data and model variances. Less damping and fewer inversion iterations can result in the same data- and model-variance pairs as the higher parameters in the trade-off curves without visible changes of the velocity-perturbation pattern. The main features of the tomographic images after the second and third iterations remain unchanged, which argues for the stability of the solution. Considering the inversion computational burden with the large amount of the P+PKP data, we chose velocity perturbations after the second iterations. The difference between the estimate of data error and standard deviation of the final residuals (~0.2 s) can be explained by well-known limitations of the isotropic teleseismic travel-time tomography, e.g., imperfect crustal corrections, velocity-model simplification or the neglect of anisotropy.

There are several options to measure and visualize the velocity perturbations and assess their reliability. A very common and simple way is to count rays passing through each grid cell, i.e. “hit-count” (Nhit). A better alternative is a “derivative weighted sum,” which considers lengths of the ray segments in each cell. Furthermore, diagonal elements of the resolution matrix (RDE)

$$R = (A^T W_D A + \varepsilon^2 W_M)^{-1} A^T W_D A \quad (3)$$

also incorporate the spatial orientation of the rays and are thus represent comprehensively how closely a particular estimate of the model parameters fits the true solution [Menke, 1984]. For qualitative insight into the ray distribution, which emphasizes the importance of how the rays intersect within grid cells, we also display the rays in depth-slices with color-coded back-azimuths (see Figure 7b in next section).

5. Results

Figure 6 shows velocity perturbations in horizontal slices at different depths of the P+PKP₃₀ velocity model. Hit counts and diagonal elements of the resolution matrix are shown in supporting information Figure S1. Variance reduction of the model is 33%. Only the nodes hit by more than 30 rays (supporting information Figure S1) are visualized in the plots. Based on synthetic tests, regions with RDE >0.7 and sufficient number of intersecting rays are considered as well-resolved.

All layers show smooth lateral variations of the velocity perturbations without taking fluctuations of positive-to-negative values at cell-size scale. Moving the center of the grid node does not affect the pattern of perturbations. Perturbations at 20 km depths reflect some uncompensated velocity heterogeneities in the crust and uncorrected variations of Moho depths. Perturbations at 50 km depth represent velocity variations in the topmost upper mantle (35–65 km). The ER separates the low-velocity perturbations beneath the ST on one side and the high-velocity perturbations beneath the TB and MD on the other side.

To verify the existence of a plume-like structure, we map expected low-velocity perturbations at the upper-mantle depths. The low-velocity perturbations cover a broad vicinity of the ER (Figure 6) at the 80 km depth, being the most significantly low south of the EG structure, beneath which the LAB shallows at least to ~80 km [Plomerová and Babuška, 2010]. The high-velocity perturbations beneath the southern BM correspond to a thicker lithospheric domain of the MD mantle, thrust beneath the TB [e.g., Babuška and Plomerová, 2013]. In slices at 110 and 140 km depths, the low-velocity perturbations concentrate around the southwestern end of the EG (~12.5E 50N) and the western part of the TB unit. Below these depths, the low-velocity perturbations shift to the NE and weaken. The high-velocity perturbations in the southern BM, distinct between 80 and 140 km node depths, continue deeper. The high-velocity perturbations prevail in the lowermost three layers of the model also in the western part of the BM, but partly lying out of the contoured well-resolved region which shifts toward the NE due to prevailing number of rays from the NE (Japan, Kuriles). Amplitudes of the velocity perturbations decrease with increasing depth, in general, and the negative perturbations do not exhibit a distinct concentration solely beneath the south-western end of the EG. If a plume-like structure is present, then the low-velocity perturbations should continue through all the depth slices, which is not the case.

Gross features imaged in shear-velocity perturbations, retrieved separately from the Q and T components of shear-waves are similar to those retrieved from the P+PKP waves (Figure 6; supporting information Figures S2 and S3). The relatively broad region of lower velocities around the center of the array (50N 12.5E) can be traced without interruption down to ~125 km and ~170 km in the SQ and ST models, respectively. The differences in perturbations between the two shear-wave models can be attributed to differences in ray-path distribution as well as to the lower number of rays (~10% each compared to number of P+PKP rays), and also to effects due to neglect of anisotropy. To constrain the shear isotropic velocity-perturbation models by the largest amount of data and improved azimuthal coverage, we inverted the combined SQ and ST data sets with the same parameters that were used for the separate ST and SQ inversions. Thanks to better coverage the area of well-resolved cells is slightly larger in the resulting SQ+ST model, but distribution of velocity perturbations does not change (supporting information Figure S4). This means that the isotropic velocities are resolved well in the shear models. No tube-like low-velocity anomaly appears to be required by the data.

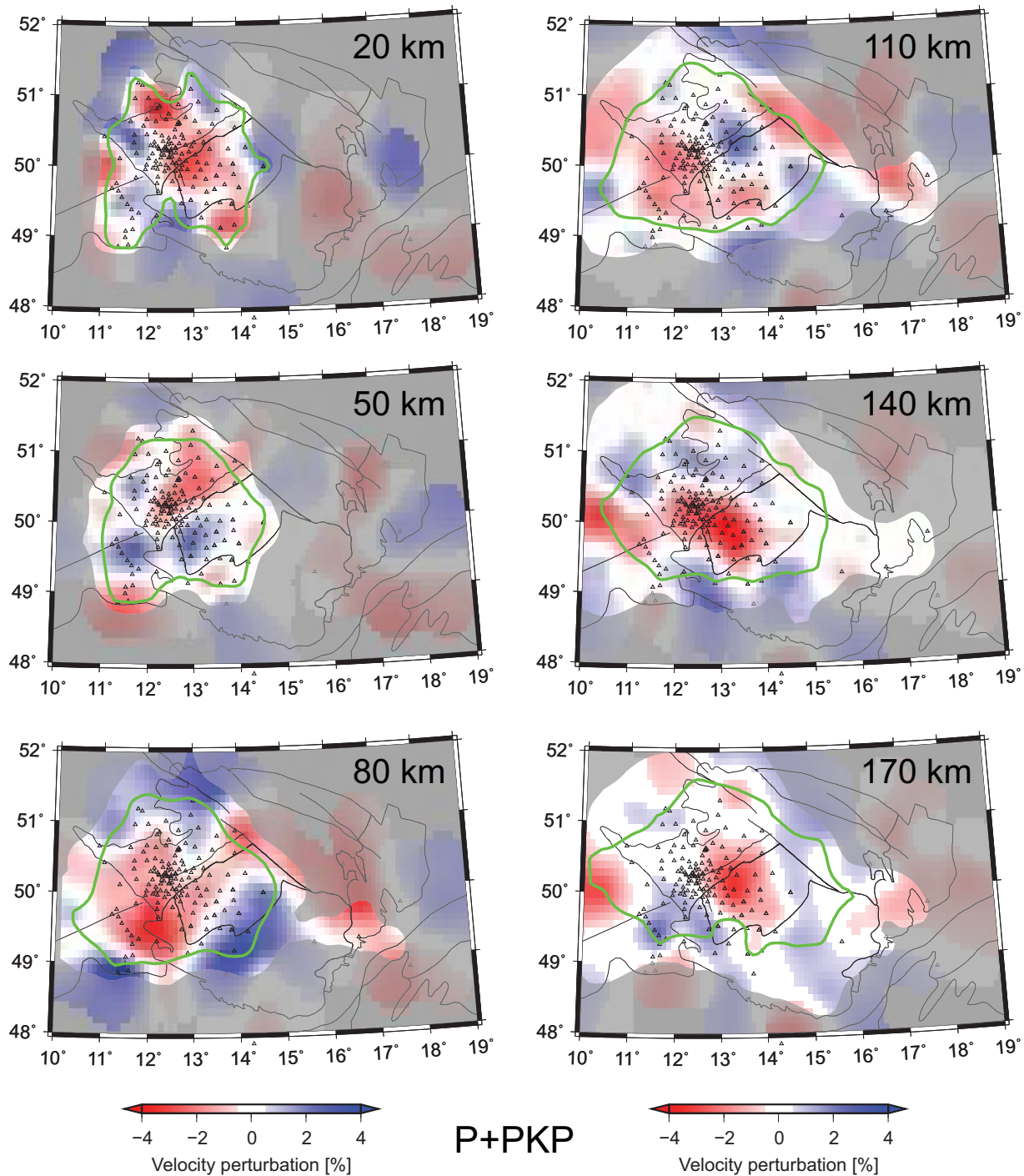


Figure 6. Plane views of v_p velocity perturbations down to 350 km in a model with 30 km vertical node spacing. Well-resolved regions with $RDE \geq 0.7$ are contoured (green), regions with $RDE \leq 0.5$ are shaded. See also supporting information Figure S1.

To assess similarities and/or differences between the velocity-perturbation models in the well-resolved parts, we show jointly the perturbations at three slices in the upper mantle along with ray-path distribution (Figure 7). We use the same scales to compare P and S tomography, though perturbation amplitudes in S tomography are larger. Assuming the same damping parameters and constant Poisson's ratio, one can expect that the relative velocity perturbations are of the same level in both the P and S-wave tomography. Then theoretically, travel-time residuals of S waves should approximately double the residuals of P waves. However in practice, the S-wave residuals are about ~ 3 times larger than the P residuals. The remaining

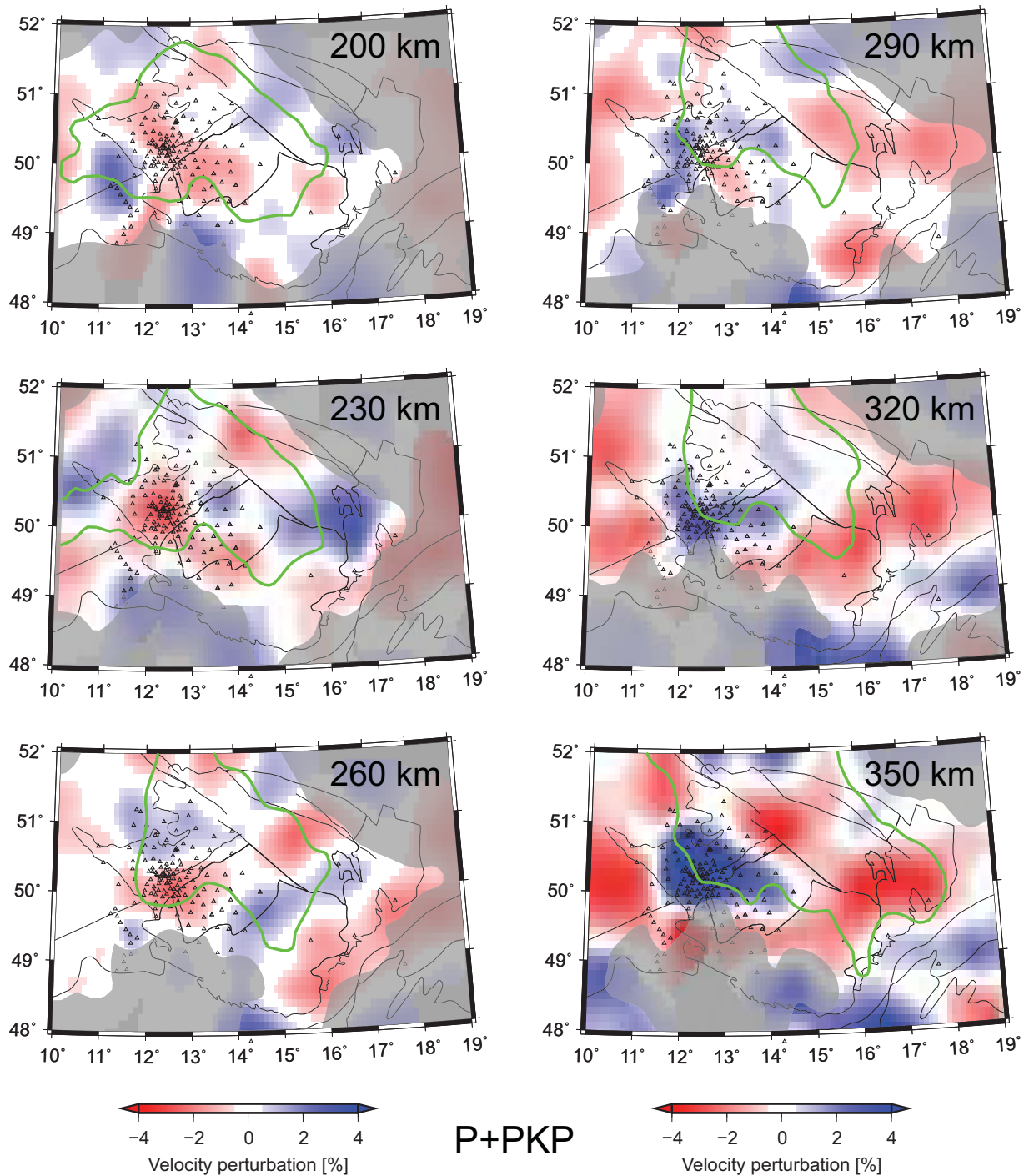


Figure 6. (continued)

~1/3 of the unexplained S residuals might relate to, e.g., larger picking errors, different ray paths, neglecting anisotropy, and variations in Poisson ratio.

A broad area of lower velocities around the center of the array at 12.5E 50N appears in all three types of tomography images in the 80 km depth slices. Differences between the P and S results appear at 125 km depth, but the general features persist. The low-velocity perturbations below the central part of the array, around the ER and MLF crossing (SW end of the EG), can be traced in all the models. The low-velocity

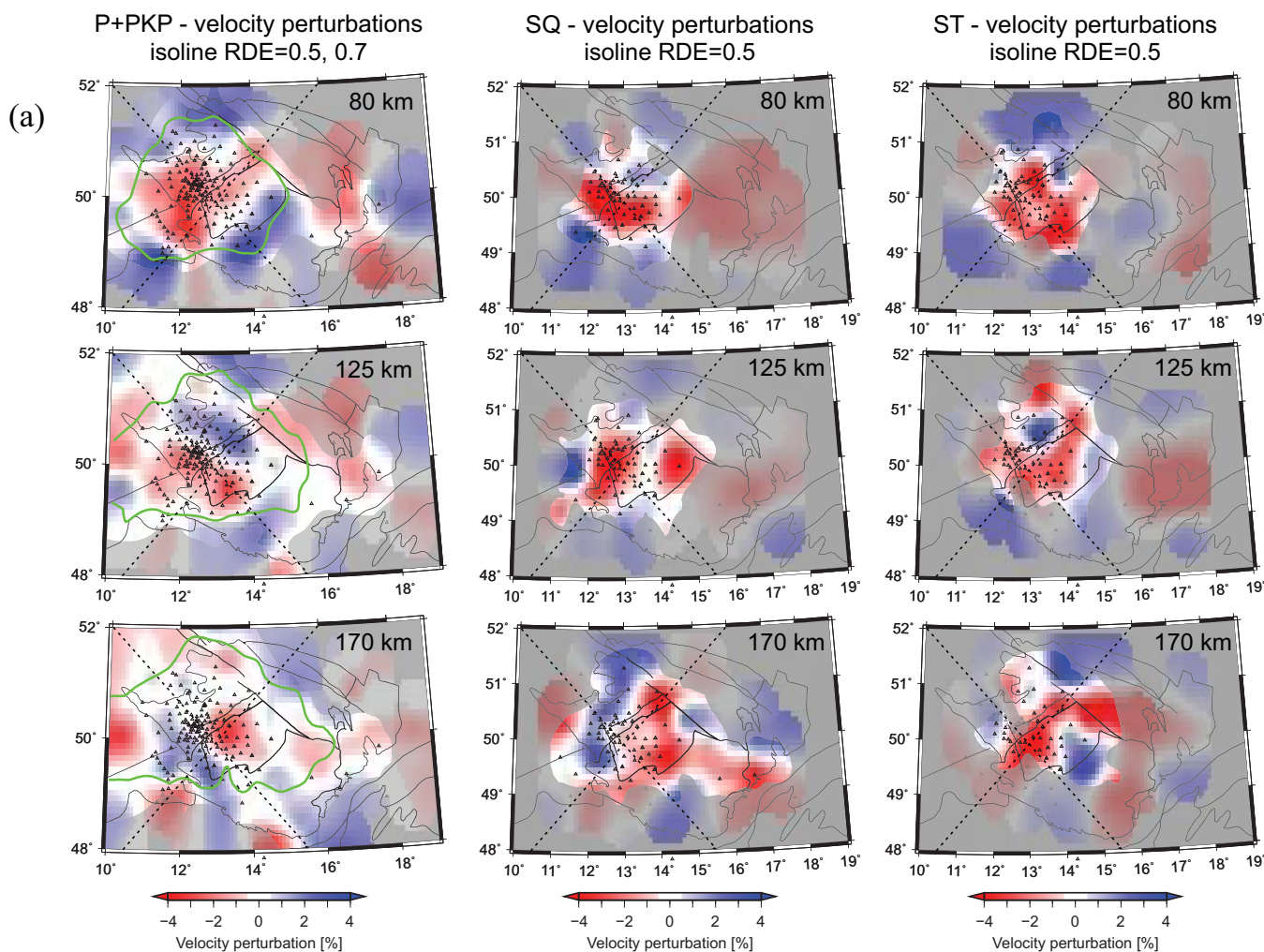


Figure 7. Comparison of v_p and v_s velocity perturbations in (a) three depth slices in models with 45 km vertical node spacing derived from three data sets: P+PKP, SQ and ST waves (b) along with ray-path distribution. Well-resolved regions of P+PKP model are contoured ($RDE \geq 0.7$; green), less well-resolved ones are shaded ($RDE \leq 0.5$). Dashed lines mark cross sections shown in Figure 8.

perturbations are larger in extent and amplitude in the central parts of the SQ and ST models. The NE shift of the low-velocity anomalies, i.e., toward the center of the BM, is evident both in the P+PKP₄₅ and SQ tomographic images at depths of 170 km. The anomalies occupy a large portion of the mantle beneath the TB unit, particularly in the SQ images. Perturbations in the P-wave tomographic model are less distinct in comparison with the upper layers, while both in the SQ and ST models the amplitudes of perturbations are similar.

Two cross sections through the three velocity-perturbation models are drawn along profiles, which cut the major low-velocity anomaly and image its depth extent (Figure 8, see also Figures 2 and 7). The anomaly is 150–250 km wide and it can be traced without interruption down to ~ 200 km in the S tomography. In the P+PKP tomography the region of the velocity decrease seems to be thinner (150–200 km), but it can be traced deeper (down to ~ 300 km). Steeper incidence for the rays in the P tomography can result in larger vertical smearing in comparison with the S tomography, but tomography based on ST shows a deeper extent of low-velocity perturbations. The region with low-velocity perturbations extends down to the same depth beneath the crossing of both profiles in all three tomography outputs (see squares in Figure 8). The low-velocity anomaly appears narrower beneath profile AB, while it is fragmented and broad beneath profile CD.

We performed several synthetic tests to assess resolution capability of the BOHEMA network (Figure 9, see also Figure 10b). Positive and negative perturbations alternate in the synthetic velocity model we test

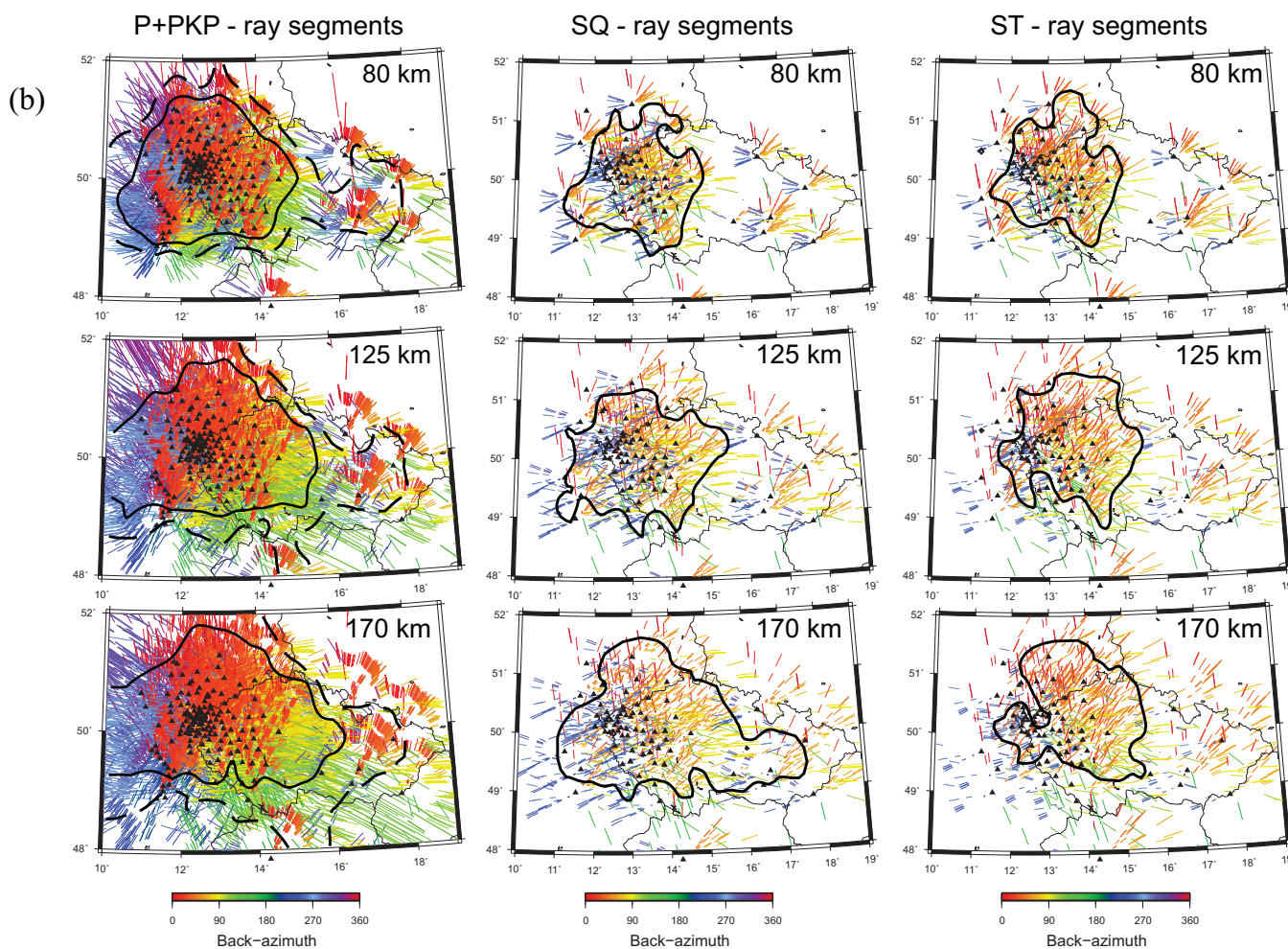


Figure 7. (continued)

(A and B velocity-perturbation patterns, Figure 9). Results for the P+PKP₃₀ station-event distribution show that tomography returns the synthetic perturbations reliably within well-sampled parts of the model (see also supporting information Figure S1). A slight smearing of the perturbations into depth levels without prescribed synthetic anomalies reflects the typical characteristic of teleseismic body-wave tomography.

6. Discussion

6.1. Plume or Asthenosphere Upwelling?

There are two competing scenarios to explain the upper mantle structure beneath the western BM: (1) existence of a “baby-plume,” similar to those modeled beneath the French Massif Central (MC) [Granet *et al.*, 1995] and Rhenish Massif (RM) [Ritter *et al.*, 2001] and (2) the lithosphere thinning, i.e., asthenosphere upwelling beneath the Eger Rift in the western BM [Plomerová *et al.*, 1998, 2007]. Low-velocity perturbations imaged in the P- and S-wave tomography of the upper mantle can help to answer which of the two scenarios is more probable.

Exploring the low-velocity perturbations in the western BM with the aim to support or to exclude the existence of a potential baby plume, we concentrate on detecting a narrow subvertical low-velocity anomaly having a diameter about 50 km. We have constructed several “tectonic” cross sections along and across the ER, to visualize in 3D the velocity perturbations in the P and S models and compared them with images of a

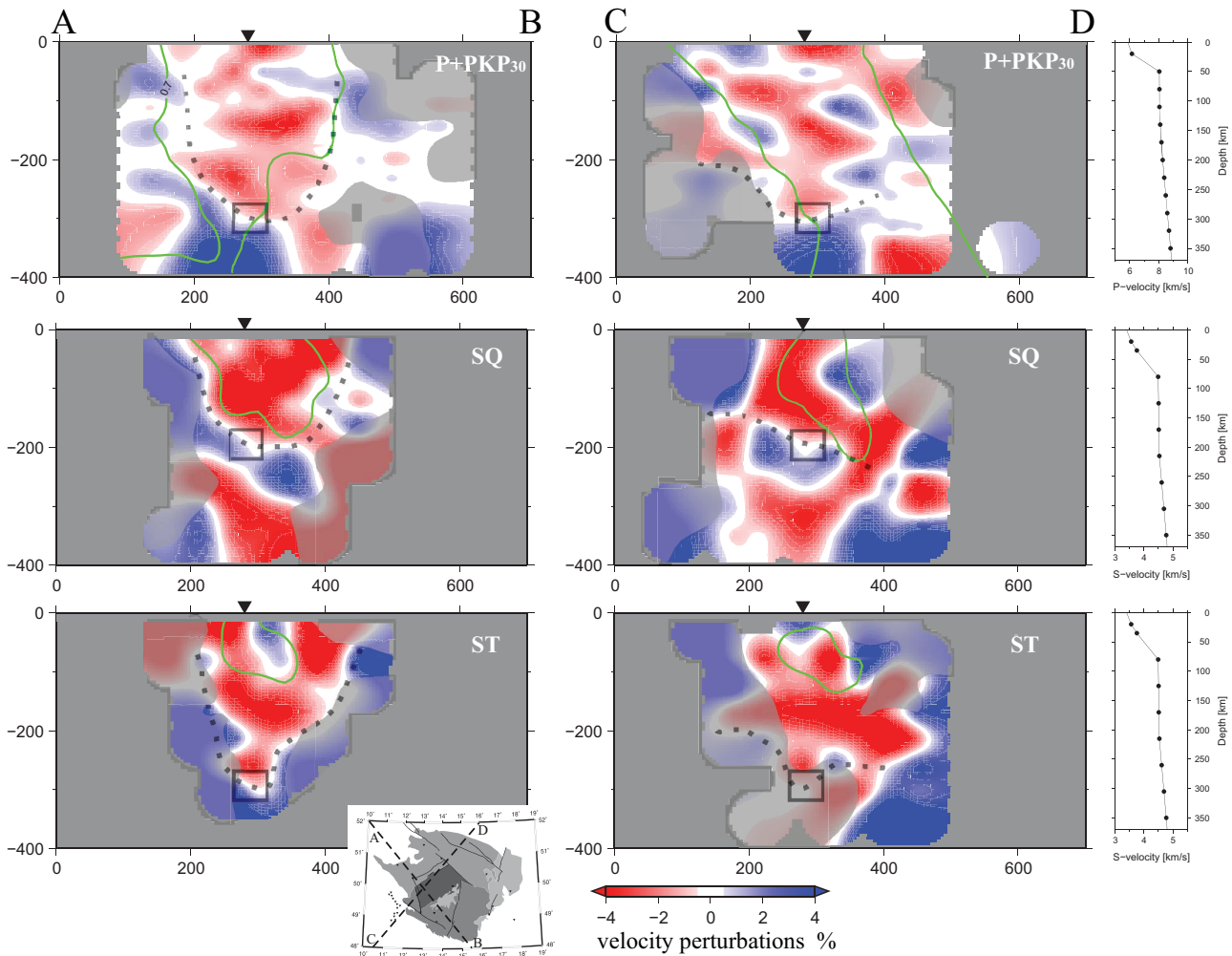


Figure 8. Cross sections through the velocity perturbation models along the AB and CD profiles (for locations see also Figures 2b and 7) cutting the most distinct anomalies. Perturbations with “hit-count” $N_{hit} \geq 30$ and $N_{hit} \geq 10$ are plotted in the P and S tomography, respectively. Regions with $RDE \leq 0.5$ are dimmed, regions with $RDE \geq 0.7$ are contoured (green). Region of continuous lower velocities is schematically marked by dotted curves. Rectangles mark its depth extend beneath point of profile crossing (triangles).

synthetic plume (Figure 10 and supporting information Figure S4). Though resolutions of the P and S models differ, the images show similar features (see also Figure 7). They display a ~ 200 km zone of low-velocity perturbations interrupted at depths near 150–200 km. The zone is most distinct beneath the central sections (Figure 10a), crossing the western ER. It is fragmented in the other two cross sections (supporting information Figure S4). The upper boundary of the low-velocity perturbations can be related to the shallow LAB, modeled below the western ER at ~ 80 km [e.g., Plomerová and Babuška, 2010].

Figure 10b shows a cross section through a synthetic model mimicking a low-velocity plume designed in analogy with those imaged by teleseismic body-wave tomography beneath the French Massif Central [Granet et al., 1995] or Rhenish Massif [Ritter et al., 2001]. The inversion was calculated from synthetics for the P+PKP station-event configuration and assumes a 2% velocity reduction relative to the IASP’91 reference model in a 60 km wide vertical column. The low-velocity perturbations from the synthetics occupy a narrow vertical volume identified only in the middle section crossing the triple junction of the ST/TB/MD units in the western end of the ER. In contrast to that, the observed low-velocity perturbations occupy about four times broader fragmented volume without a clear and indisputable link to deeper parts of the mantle, where a common source feeding the “baby plumes” was suggested [Granet et al., 1995; Goes et al., 1999]. An interpretation of the lower velocities in the upper mantle beneath the western BM as reflecting a “baby plume” thus seems unlikely.

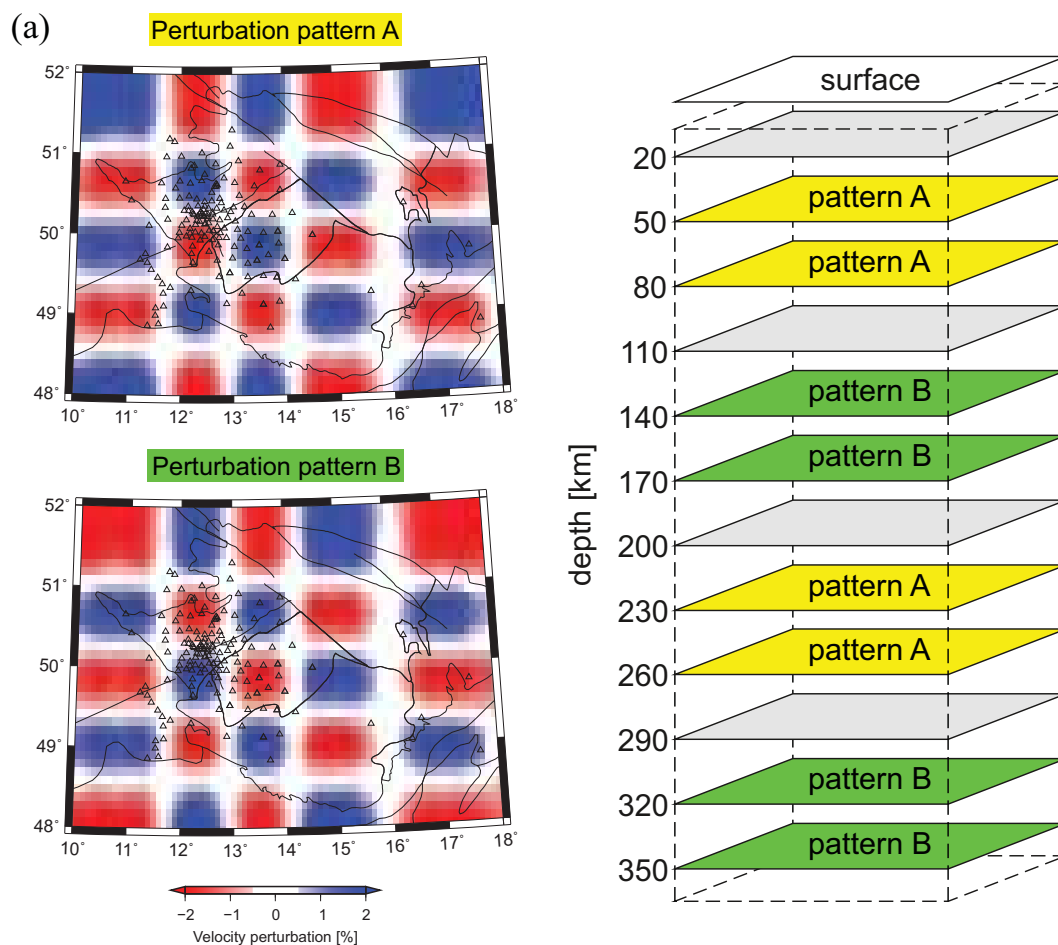


Figure 9. Checkerboard test of the array resolution for (a) synthetic model and (b) recovered velocity perturbations.

Already initial regional inversions for P-velocity structure [Plomerová *et al.*, 2007] did not show any narrow subvertical low-velocity anomaly in the upper mantle beneath the western BM. That preliminary tomography used 90% of the P-wave arrival times of the present P-wave set (without the PKP phases) with residuals in a range of (−0.7 s, 0.7 s). At first glance, the resulting models presented in this study differ from the preliminary 2007 model (supporting information Figure S5), though they both effect 33% data-variance reduction. However, if we restrict the comparison to the well-resolved parts of the new model and take into consideration differences in the residual preprocessing, the crustal corrections applied, the model parameterizations and inversion regularization, as well as the graphical visualizations [Plomerová *et al.*, 2007], the general features of both models are similar (supporting information Figure S6). We attribute the diffuse pattern of small alternating negative and positive perturbations in the shallow layers of the preliminary model mainly to shortcomings of the “layer-stripping” approach [Evans and Achauer, 1993] used to correct for crustal effects and to the narrower travel-time-residual range. Uncorrected remnants of crustal heterogeneities might be mapped into the upper mantle [Karousová *et al.*, 2012a] in the earlier model. The broad low-velocity anomaly around the ER and higher velocities beneath the Moldanubian unit are clearly visible in both models, though they are more fragmented in the 2007 model. At 110 km depth, the separation of negative and positive perturbations in the SW and NE of the ER is less evident in the 2007 model. Perturbations in the deeper layers of the 2007 model with larger cells are smoother and exhibit high coherence with large-scale features of the model presented in this paper. The perturbation pattern (this paper) reflects the complex structure of the upper mantle in the western BM, whose mantle lithosphere is composed of several domains with differently oriented fabrics [e.g., Babuška and Plomerová, 2013].

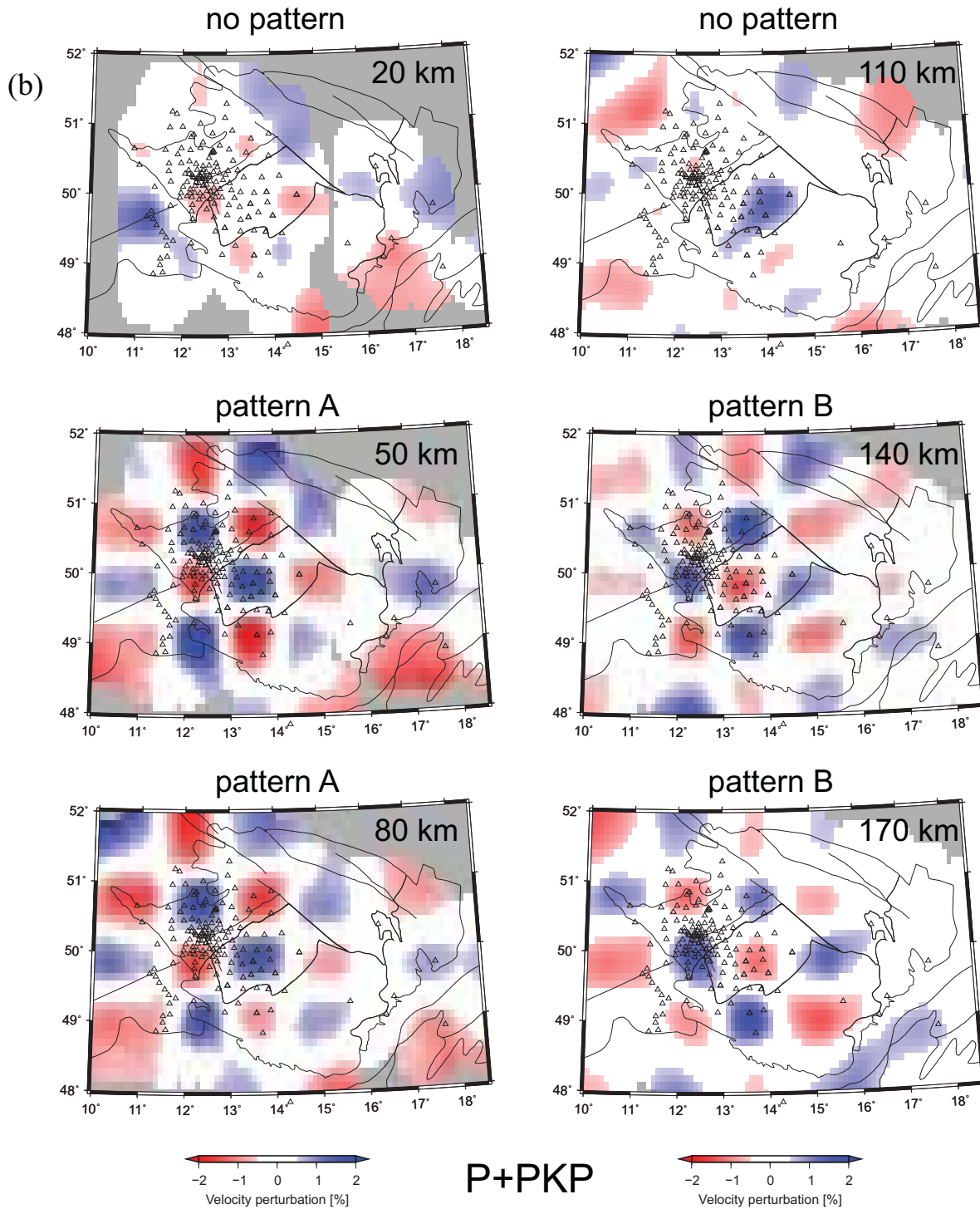


Figure 9. (continued)

The full-waveform tomographic velocity model of the European mantle by *Fichtner and Villaseñor* [2015] has much less vertical smearing than the body-wave teleseismic tomography. This model images several localized low-velocity anomalies that can be related to the ECRIS. The low-velocity regions, including one beneath the BM, are confined to the upper 200 km of the mantle, with distinct velocity minima beneath centers of tectonic and volcanic activity. If plumes existed below the 300 km depth, then their diameters

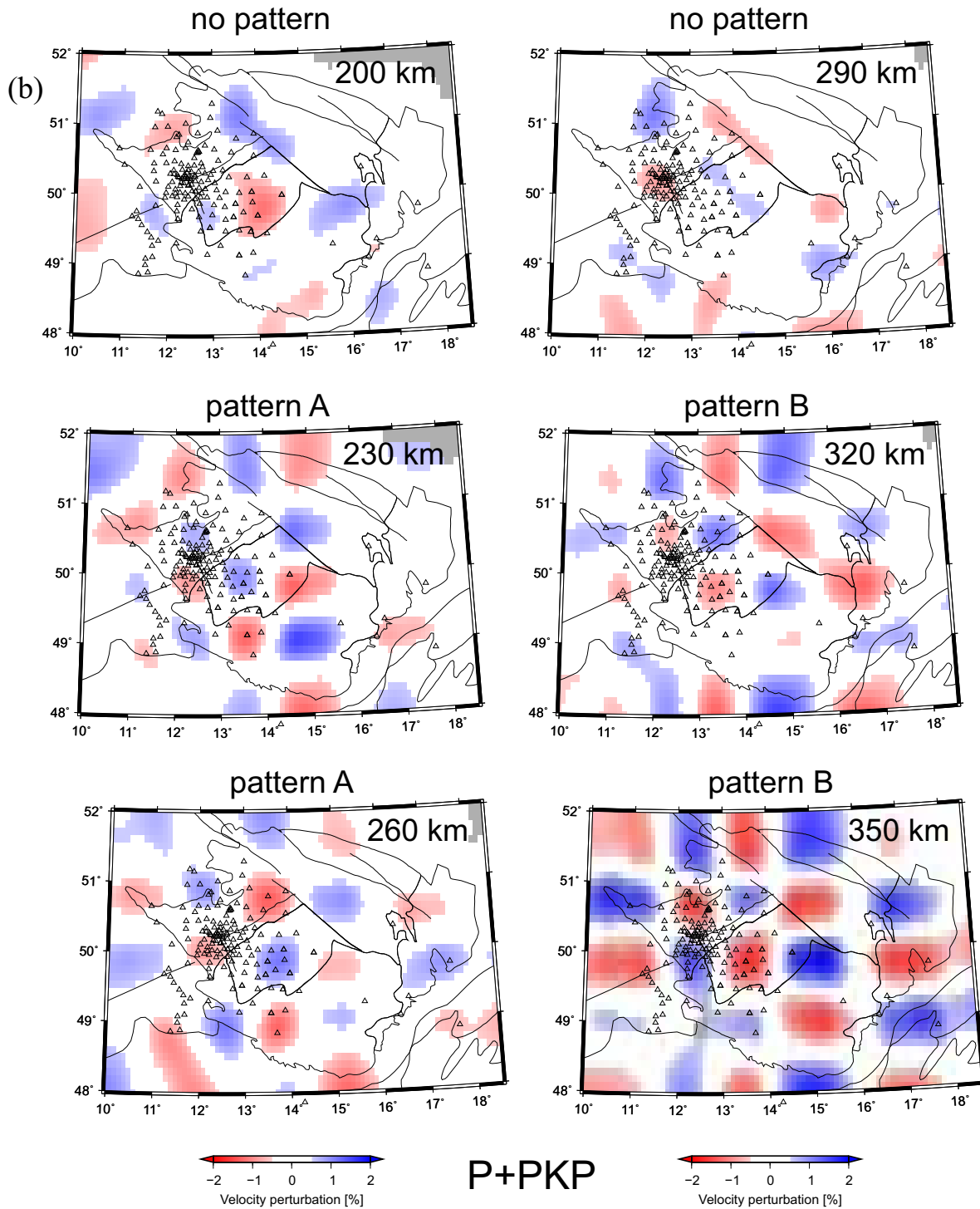


Figure 9. (continued)

would have to be smaller than ~ 100 km to remain seismically invisible. Because full-waveform inversions do not show clear evidence for mantle plume beneath central and western Europe, a common deep-mantle source of volcanism along the ECRIS seems to be implausible.

The results of the P and S tomography presented in this paper thus support the alternative explanation of the lower velocities detected beneath the western part of the BM, i.e., by the shallowing the lithosphere-

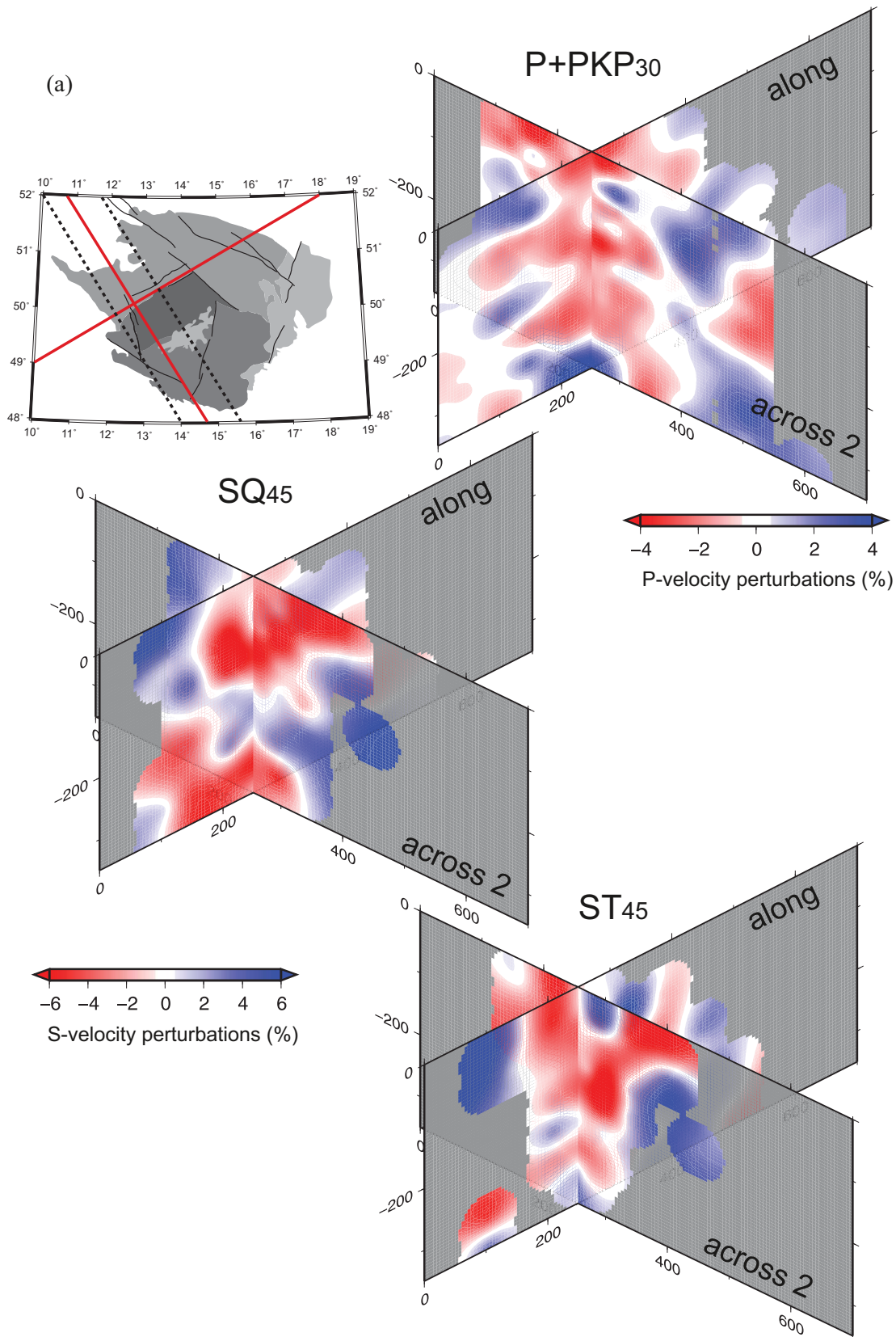


Figure 10. Cross sections through the velocity perturbation models along “tectonic” profiles (a) oriented parallel and across the Eger Rift (see also supporting information Figure S5); (b) cross section cutting the model of a synthetic plume modeled as 2% low-velocity anomaly of 60 km width in analogy with the plumes in the French Massif Central and Eiffel.

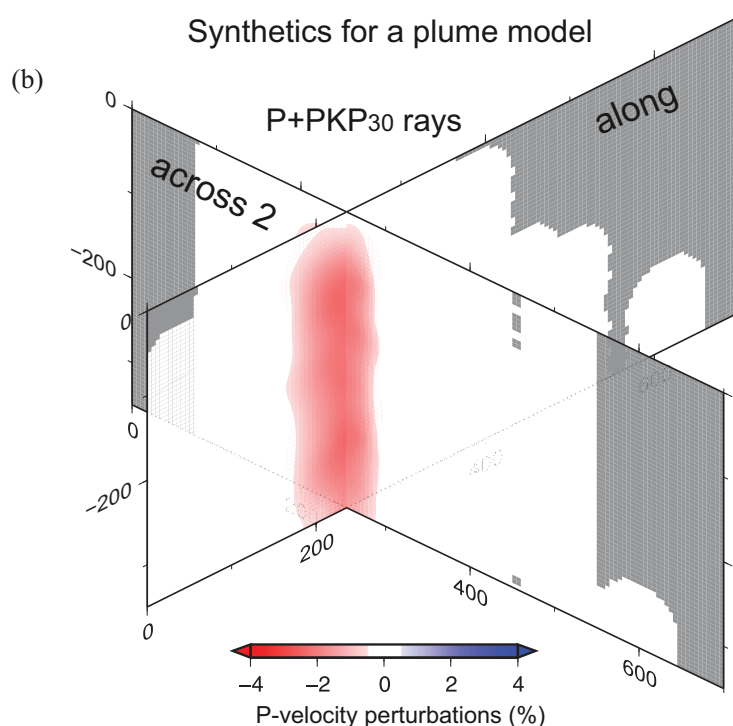


Figure 10. (continued)

asthenosphere boundary beneath the ER [Plomerová *et al.*, 1998, 2007]. The corresponding LAB upwelling was also modeled by different techniques [e.g., Heuer *et al.*, 2007; Geissler *et al.*, 2007; Plomerová and Babuška, 2010]. Based on results of P receiver functions, Heuer *et al.* [2011] accepted the proposed plume-like structure in the upper mantle below the western Bohemia earthquake region [Granet *et al.*, 1995], but with no or only weak imprint on the 410 km discontinuity. On the other hand, the boundaries between mantle domains of the three tectonic units forming the lower lithosphere in the region, determined from studies of seismic anisotropy, represent weak zones in the otherwise rigid mantle lithosphere. In the past, such zones probably served as paths for upward flow of hot mantle material, which could modify the mantle domain boundaries and locally thinned their lithosphere.

The general distribution of positive and negative velocity perturbations in the upper mantle tomography in this paper correlates well with the depth-variations of the LAB reported by Plomerová and Babuška [2010]. The tomographic images show the asthenosphere upwelling along the ER and the southward thickening of the high-velocity lithosphere beneath the MD part of the BM, detectable down to 80–140 km depths (e.g., Figure 6). The detected lithosphere thinning along the WSW-ENE-trending ER fits the general orientation of the Variscan orogen in central Europe and parallels the boundaries between the ST, MD and TB lithospheric domains in the upper mantle [Babuška and Plomerová, 2006]. We interpret the mantle-lithosphere domains with consistent anisotropy fabrics as representatives of originally separated microplates, which were assembled during the Gondwana and Laurentia-Baltica collision and created the BM [Babuška and Plomerová, 2013]. Gradual stabilization of the bottom of the lithosphere took place as a result of slab break-off episodes and the erosion of the lithosphere-asthenosphere boundary by mantle flow. This erosion likely affected the weakened suture zones as well. Such process could have led to the observed LAB upwelling related to the ST and TB/MD mantle-domain contacts.

6.2. Results of BOHEMA Tomography in Light of Other Studies

Long-term seismological research, carried out in the western BM, supplied new inferences on the upper-mantle structure, especially its velocities, anisotropy, domain-like structure, discontinuities etc., and calls for a reassessment of the “baby-plume” concept suggested for Variscan Europe.

High-resolution velocity images from the BOHEMA P and S arrivals did not identify a narrow “baby-plume” beneath the BM. In the absence of the clear magma conduit that would be detectable in the present-day upper-mantle velocities it is prudent to ask why abundant volcanism spreads along the ER and from where it was fed in the past. *Amaru* [2007] combined data from permanent observatories and several temporary arrays [*Amaru et al.*, 2008], and imaged velocities down to the lower mantle. Low velocities dominate beneath central Europe at depths down to 400–600 km. Moreover, the tomography of the authors above shows a distinct vertical low-velocity zone extending from the bottom of the lower mantle to the Transition Zone. Because the perturbation weakens both in its extent and amplitude at the lower boundary of the Transition Zone, its connection with the upper mantle low-velocities is less evident. In spite of that, *Amaru* [2007] accepts the *Goes et al.* [1999] interpretation that this lower mantle upwelling is a source for the MC, RM and BM volcanism. The Bohemian Massif is the thickest of the Variscan Massifs [*Plomerová and Babuška*, 2010] and may as such have the “strongest” lithosphere which would not allow a plume of small scale and force to penetrate through the compact block. This process might end in accumulating the upwelling material at the base of the lithosphere as a kind of underplating, followed by gradual erosion of the basal lithosphere into the shape of a broadly updoming mantle anomaly.

Concentration of the low-velocity material in the sublithospheric upper mantle beneath central Europe is a striking feature in the tomography by *Amaru* [2007]. Existence of weakened zones in the lithosphere appears as a necessary condition for transport of hot molten material to the surface [*Babuška et al.*, 2002], as its transport upward through an intact rigid mantle-lithosphere block would be difficult. Boundaries between mantle-lithosphere domains, delimited from large-scale seismic anisotropy, have often matched the boundaries of crustal terranes. *Babuška et al.* [2002] modeled fabrics of three sharply bounded mantle lithosphere domains beneath the MC and proposed that magmas feeding the Cenozoic volcanism, which developed on two peripheral parts of the southern thinned domain, were channeled to the Cantal and Mont Dore volcanoes by the reactivated Variscan suture hidden in the mantle.

Wilson and Downes [2006] deduce from distribution of the low-velocity anomalies beneath the MC and RM [*Granet et al.*, 1995; *Ritter et al.*, 2001] that they do not seem to be rooted in the lower mantle, though they might extend down to the Transition Zone. A positive thermal anomaly at the Transition Zone depths, which could be related to the hotter low-velocity material reservoir in the mantle, is absent. Instead, the location of the plume-like structure actually correlates with a zone of high-velocity material within the Transition Zone reflecting accumulation of subducted slabs. The authors proposed the low-velocity anomalies could be products of localized fluid streaming from the top of the Transition Zone.

Walker et al. [2005] interpret shear-wave splitting in the Rhenish Massif by a parabolic asthenospheric flow and use optimum model parameters to calculate Eurasian plate speed at 12 km/Ma. Their model is consistent with geological, tomographic, receiver function, electrical conductivity anisotropy and geochemical findings in the Eifel region, as well as with global absolute plate motion, whose speed is estimated at 19 ± 14 km/Ma in the HS3-NUVEL1A [*Gripp and Gordon*, 2002]. Indeed, ages of volcanic centers are very different. Volcanism is dated back to 28 Ma on the east (the southern Leine Graben), while it is much younger (from 2.7 Ma to recent) in the central part of the RM (the southern Ruhr Graben). The plume structure manifested clearly in tomography by *Ritter et al.* [2001] down to the top of the Transition Zone splits at depths of around 50 km. The eastern shallow anomaly, without an evident connection to the deeper parts, may represent remnants of the older volcanism terminated about 5 Ma ago. Extension related to the Leine Graben rifting weakened further the contact of the Rhenohercynian (RH) and ST mantle lithosphere domains and enabled sublithospheric mantle upwelling along the Rhenic Suture. The younger volcanism further to the west is fed with the hot mantle material transported to the surface most probably along the same suture opened (weakened) by the extension related to the rifting below the Ruhr Graben.

6.3. Rifts, Sutures, and Volcanism Distribution

In general, the centers of the Tertiary to Quaternary volcanism linked to the ECRIS concentrate mostly at the ends of the rifts, close to distinct tectonic sutures cutting the rifts at high angles, e.g., the Limagne Graben (LiG) in the Massif Central (MC) and the Moldanubian Suture (MD), or, the Ruhr (RhG) and Leine (LeG) Grabens in the Rhenish Massif (RM) and the Rhenic Suture (Figure 11a). In the Eger Rift (ER), the volcanism is not restricted to the graben structure (EG) which is parallel the Saxothuringian/Teplá-Barrandian Suture. It extends to the southwest, beyond the Mariánské-Lázně Fault (MLF), and to the northeast, beyond the Elbe

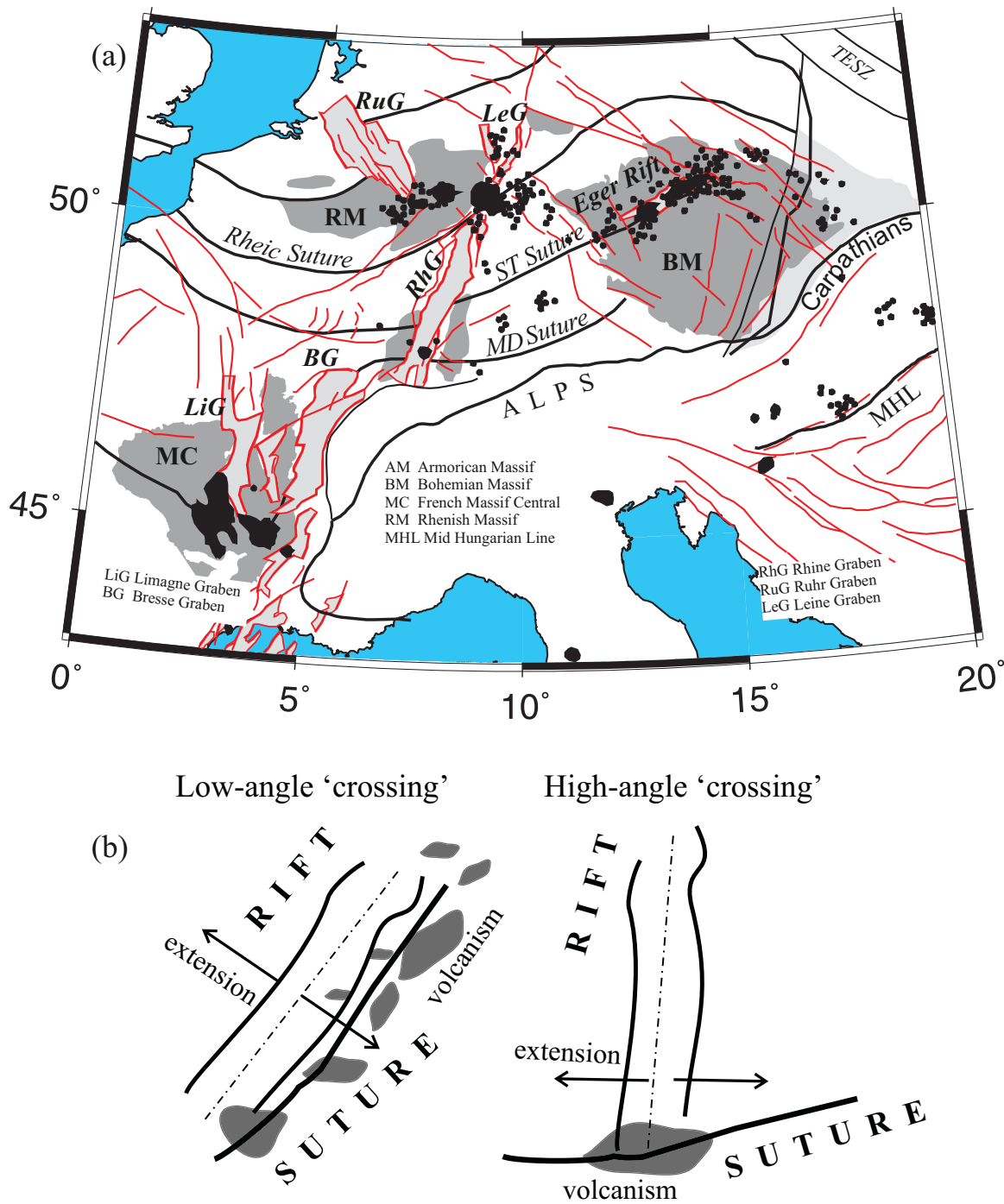


Figure 11. (a) ECRIS and related Cenozoic volcanism and (b) schematic presentation of the low- and high-angle rift and suture "crossing."

Fault Zone (EFZ). Both fault zones limit the graben structure (EG) of the presumably longer Eger Rift (Figure 2). The EFZ and the Sudetic faults (ISF, SMF) seem to be responsible for volcanism taking place in the northern part of the BM.

The broadly spread volcanism along the ER might reflect differences in orientation of the structures and acting extensional stresses (Figure 11b). Alignment of the rift elongation axis (perpendicular to the rift extension) and the deep mantle lithosphere suture between the ST and TB/MD resulted in weakening of a longer segment of the ST Suture and thus in opening of a larger portion of the rift for ascent of the hot volcanic

mantle material to the surface. The orientation of the rift axis and the suture in the mantle lithosphere seems to be responsible for either a widely distributed volcanism (in case of subparallel orientation) or for creating a localized volcanic center (in case of a high-angle orientation). This may explain why no narrow and steep, finger-like low-velocity anomaly similar to those modeled beneath the MC and RM has been imaged beneath the ER in the western BM. Only short segments of the RH/ST and MD sutures were likely weakened by extensional stresses of the rifts in the MC and RM (Figure 11). These two short segments of the sutures might thus be apt to appear as “circular” conduits for hot material escaping episodically from the mantle to the surface.

Babuška and Plomerová [2010] suggested that the sublithospheric mantle beneath the western BM acted as a major source for heat and partial melts. Variscan boundaries in the brittle lithospheric-mantle domains served as magma conduits for the late-orogenic granitic magmatism and, after rejuvenation of some of them, also for the Cenozoic volcanism. It is likely that some of the so-called intra-plate phenomena can be related to partly healed, and later rejuvenated, micro-plate boundaries. The upward flow of the hot mantle material could penetrate along the boundaries from deeper parts to the surface, modify the domain boundaries and/or thin the domains. Orientation of lithosphere domain boundaries in the mantle and extensional forces in the rifts seems to play important role in distribution of volcanism. Mantle processes in general, appear to be decisive for various near-surface features or geological characteristics observed on the surface.

7. Conclusions

By inverting body-wave travel-time residuals we have shed light on the question regarding the general validity of the well-known “baby-plume” concept in central European provinces with Cenozoic volcanism, particularly in the western Bohemian Massif. High-resolution P- and S-wave velocity tomography based on data recorded during the BOHEMA passive seismic experiment show that velocity-perturbation patterns in the P- and S-wave models exhibit similar features, in general, though their resolutions are different. None of the models display a clear “plume-like” structure, i.e., a narrow subvertical low-velocity anomaly, neither below the western Eger Rift, nor below other parts of the BM. This finding is in accord with results of the full-waveform inversion which did not image mantle plumes beneath Europe, that could be responsible for the ECRIS [*Fichtner and Villaseñor*, 2015].

A 200 km wide zone of low-velocity perturbations beneath the western BM seems to be interrupted in the velocity models of present-day upper mantle at depths of ~150–200 km, indicating no or a very weak connection of the zone with a potential magma reservoir at greater depths. The low-velocity zone is most distinct beneath the western end of the graben structure of the ER and it is fragmented in the remaining segments of the rift. The broad shape of the anomaly and the lack of evident connection with deeper parts of the mantle support our interpretation of such low-velocity anomaly in the western BM by a lithosphere thinning along the Eger Rift. An upward flow of hot mantle material could penetrate in the past along boundaries of the mantle lithosphere domains from the sublithospheric mantle to the surface, modify the domain boundaries and/or thinned the lithosphere. Upper boundary of the low-velocity perturbations can be related to the shallow LAB, modeled below the western ER at ~80 km [e.g., *Plomerová and Babuška*, 2010].

Results of several seismic velocity-tomography studies indicate broadly dispersed low-velocities, indicative of hot buoyant upper mantle beneath central Europe. Processes that transported the hot material actively, either in the past, or at present, hardly could “drill” upward through the compact rigid block of the mantle lithosphere. More likely, an episodic transport of the material happened along weakened zones between the blocks. Boundaries of the mantle lithosphere domains, manifested at the surface as distinct sutures can serve as paths for the mantle material transport to the volcanic centers, particularly, if the collisional zone between the domains was weakened due to extensional processes. The rift extension at a high angle to a suture might allow extrusion of the volcanic material along the entire rift, whereas extension subparallel to the suture opens only a short segment of the rift. The rifts in the French Massif Central and in the Rhenish Massif can serve as examples of the latter and the Eger Rift in the western part of the BM for the former rift-suture configuration.

Acknowledgments

Suggestions of A. Fichtner and an anonymous reviewer improved the manuscript. Special thanks go to Jeffrey Park for a critical reading of the manuscript for style and clarity. The Grant Agency of the Czech Republic supported the research by grant P210-12-2381 and the BOHEMA array operation during 2001–2003 by grant 205/01/1154. We greatly appreciate operation of five broad-band stations provided by the ETH Zürich at the early stage of the experiment, whose seismograms substantially enlarge the data sets. Data acquisition from permanent observatories was supported by the project of large research infrastructure CzechGeo/EPOS, grant LM2010008 and LM2015079. Waveforms of the events used in this study are accessible via the Institute of Geophysics, Czech Academy of Sciences seismological archive upon request.

References

- Achauer, U., and F. Masson (2002), Seismic tomography of continental rifts revisited: From relative to absolute heterogeneities, *Tectonophysics*, 358, 17–37, doi:10.1016/S0040-1951(02)00415-8.
- Aki, K., A. Christofferson, and E. S. Husebye (1977), Determination of the three dimensional seismic structure of the lithosphere, *J. Geophys. Res.*, 82, 277–296, doi:10.1029/JB082i002p00277.
- Amaru, M. L. (2007), Global travel time tomography with 3-D reference models, PhD thesis, Utrecht Univ., Utrecht, Netherlands.
- Amaru, M. L., W. Spakman, A. Villaseñor, S. Sandoval, and E. Kissling (2008), A new absolute arrival time data set for Europe, *Geophys. J. Int.*, 173, 465–472, doi:10.1111/j.1365-246X.2008.03704.x.
- Babuška, V., and J. Plomerová (2006), European mantle lithosphere assembled from rigid microplates with inherited seismic anisotropy, *Phys. Earth Planet. Inter.*, 158, 264–280, doi:10.1016/j.pepi.2006.01.010.
- Babuška, V., and J. Plomerová (2010), Mantle lithosphere control of crustal tectonics and magmatism of the western Ohře (Eger) Rift, *J. Geosci.*, 55, 171–186, doi:10.3190/jgeosci.070.
- Babuška, V., and J. Plomerová (2013), Boundaries of mantle-lithosphere domains in the Bohemian Massif as extinct exhumation channels for high-pressure rocks, *Gondwana Res.*, 23, 973–987, doi:10.1016/j.gr.2012.07.005.
- Babuška, V., J. Plomerová, and J. Šílený (1987), Structural model of the subcrustal lithosphere in central Europe, in *The Composition, Structure and Dynamics of the lithosphere-Asthenosphere System*, *Geophys. Ser.*, edited by C. Froidevaux and K. Fuchs, pp. 239–251, AGU, Washington, D. C.
- Babuška, V., J. Plomerová, L. Vecsey, M. Granet, and U. Achauer (2002), Seismic anisotropy of the French Massif Central and predisposition of Cenozoic rifting and volcanism by Variscan suture hidden in the mantle lithosphere, *Tectonics*, 21(4), 1029, doi:10.1029/2001TC901035.
- Babuška, V., J. Plomerová, and L. Vecsey (2008), Mantle fabric of western Bohemian Massif (central Europe) constrained by 3D seismic P and S anisotropy, *Tectonophysics*, 462, 149–163, doi:10.1016/j.tecto.2008.01.020.
- Bankwitz, P., G. Schneider, H. Kämpf, and E. Bankwitz (2003), Structural characteristics of epicentral areas in Central Europe: Study case Cheb Basin (Czech Republic), *J. Geodyn.*, 35, 5–32, doi:10.1016/S0264-3707(02)00051-0.
- Bräuer, K., H. Kämpf, S. Niedermann, and G. Strauch (2005), Evidence for ascending upper mantle-derived melt beneath the Cheb basin, central Europe, *Geophys. Res. Lett.*, 32, L08303, doi:10.1029/2004GL022205.
- Čermák, V. (1994), Results of heat flow studies in Czechoslovakia, in *Crustal Structure of the Bohemian Massif and the West Carpathians*, edited by V. Bucha and M. Blížkovský, pp. 85–120, Springer, Berlin.
- Chang, S. J., S. van der Lee, M. P. Flanagan, H. Bedle, F. Marone, E. M. Matzel, M. E. Pasyanos, A. J. Rodgers, B. Romanowicz, and Ch. Schmid (2010), Joint inversion for three-dimensional S velocity mantle structure along the Tethyan margin, *J. Geophys. Res.*, 115, B08309, doi:10.1029/2009JB007204.
- Dando, B. D. E., G. W. Stuart, G. A. Houseman, E. Heged, E. Brückl, and S. Radovanovi (2011), Teleseismic tomography of the mantle in the Carpathian–Pannonian region of central Europe, *Geophys. J. Int.*, 186, 11–31, doi:10.1111/j.1365-246X.2011.04998.x.
- Dezes, P., S. M. Schmid, and P. A. Ziegler (2004), Evolution of the European Cenozoic Rift System: Interaction of the Alpine and Pyrenean orogens with their foreland lithosphere, *Tectonophysics*, 389, 1–33, doi:10.1016/j.tecto.2004.06.011.
- Díaz, J., J. Gallart, I. Morais, G. Silveira, D. Pedreira, J.A. Pulgar, N.A. Dias, M. Ruiz, and J.M. González-Cortina (2015), From the Bay of Biscay to the High Atlas: Completing the anisotropic characterization of the upper mantle beneath the westernmost Mediterranean region, *Tectonophysics*, 663, 192–202.
- Evans, J. R., and U. Achauer (1993), Teleseismic velocity tomography using the ACH method: Theory and application to continental scale studies, in *Seismic Tomography*, edited by H. M. Iyer and K. Hirahara, pp. 319–360, Chapman and Hall, London, U. K.
- Fichtner, A., and A. Villaseñor (2015), Crust and upper mantle of the western Mediterranean—Constraints from full-waveform inversion, *Earth Planet. Sci. Lett.*, 428, 52–62, doi:10.1016/j.epsl.2015.07.038.
- Franke, W. (2006), The Variscan orogeny in Central Europe: Construction and collapse, in *European Lithosphere Dynamics, Memoirs*, vol. 32, edited by D. G. Gee and R. A. Stephenson, pp. 333–343, Geol. Soc., London, doi:10.1144/GSL.MEM.2006.032.01.20.
- Geissler, W. H., H. Kämpf, R. Kind, K. Bräuer, K. Klinge, T. Plenefisch, J. Horálek, J. Zedník, and V. Nehybka (2005), Seismic structure and location of a CO₂ source in the upper mantle of the western Eger Rift, central Europe, *Tectonics*, 24, TC5001, doi:10.1029/2004TC001672.
- Geissler, W. H., H. Kämpf, W. Seifert, and P. Dulski (2007), Petrological and seismic studies of the lithosphere in the earthquake swarm region Vogtland/NW Bohemia, central Europe, *J. Volcanol. Geotherm. Res.*, 159, 33–69, doi:10.1016/j.jvolgeores.2006.06.011.
- Geissler, W. H., H. Kämpf, Z. Skácelová, J. Plomerová, V. Babuška, and R. Kind (2012), Lithosphere structure of the NE Bohemian Massif (Sudetes)—A teleseismic receiver function study, *Tectonophysics*, 564–565, 12–37, doi:10.1016/j.tecto.2012.05.005.
- Goes, S., W. Spakman, and H. Bijwaard (1999), A lower mantle source for central European volcanism, *Science*, 286, 1928–1931, doi:10.1126/science.286.5446.1928.
- Granet, M., M. Wilson, and U. Achauer (1995), Imaging a mantle plume beneath the French Massif Central, *Earth Planet. Sci. Lett.*, 136, 281–96, doi:10.1016/0012-821X(95)00174-B.
- Gripp, A. E., and R. G. Gordon (2002), Young tracks of hotspots and current plate velocities, *Geophys. J. Int.*, 150, 321–361, doi:10.1046/j.1365-246X.2002.01627.x.
- Heuer, B., W. H. Geissler, R. Kind, and H. Kämpf (2006), Seismic evidence for asthenospheric updoming beneath the western Bohemian Massif, central Europe, *Geophys. Res. Lett.*, 33, L05311, doi:10.1029/2005GL025158.
- Heuer, B., H. Kämpf, R. Kind, and W. H. Geissler (2007), Seismic evidence for whole lithosphere separation between Saxothuringian and Moldanubian tectonic units in central Europe, *Geophys. Res. Lett.*, 34, L09304, doi:10.1029/2006GL029188.
- Heuer, B., W. H. Geissler, R. Kind, and BOHEMA Working Group (2011), Receiver function search for a baby plume in the mantle transition zone beneath the Bohemian Massif, *Geophys. J. Int.*, 187, 577–594, doi:10.1111/j.1365-246X.2011.05155.x.
- Horálek, J., and T. Fischer (2008), Role of crustal fluids in triggering the West Bohemia/Vogtland earthquake swarms: Just what we know (a review), *Stud. Geophys. Geod.*, 52, 455–478, doi:10.1007/s11200-008-0032-0.
- Hrubcová, P., and W. H. Geissler (2009), The crust-mantle transition and the Moho beneath the Vogtland/west Bohemian region in the light of different seismic methods, *Stud. Geophys. Geod.*, 53, 275–294, doi:10.1007/s11200-009-0018-6.
- Hrubcová, P., P. Šroda, A. Špičák, A. Guterch, M. Grad, G. R. Keller, E. Brueckl, and H. Thybo (2005), Crustal and uppermost mantle structure of the Bohemian Massif based on CELEBRATION 2000 data, *J. Geophys. Res.*, 110, B11305, doi:10.1029/2004JB003080.
- Jelinek, E., V. Štědrá, and J. Cháb (1997), The Mariánské Lázně complex, in *Geological Model of Western Bohemia Related to the KTB Borehole in Germany*, vol.47, edited by S. Vrána and V. Štědrá, pp. 61–70, Czech Geol. Surv., Prague.

- Kämpf, H., K. Bräuer, J. Schumann, K. Hahne, and G. Strauch (2013), CO₂ discharge in an active, non-volcanic continental rift area (Czech Republic): Characterisation ($\delta^{13}\text{C}$, 3He/4He) and quantification of diffuse and vent CO₂ emissions, *Chem. Geol.*, *339*, 71–83, doi:10.1016/j.chemgeo.2012.08.005.
- Karousová, H., J. Plomerová, and V. Babuška (2012a), Three-dimensional velocity model of the crust of the Bohemian Massif and its effects on seismic tomography of the upper mantle, *Stud. Geophys. Geod.*, *56*, 249–267, doi:10.1007/s11200-010-0065-z.
- Karousová, H., J. Plomerová, and L. Vecsey (2012b), Seismic tomography of the upper mantle velocity structure beneath the north-eastern Bohemian Massif (central Europe), *Tectonophysics*, *564-565*, 1–11, doi:10.1016/j.tecto.2012.06.031.
- Karousová, H., J. Plomerová, and V. Babuška (2013), Upper mantle structure beneath the southern Bohemian Massif and its surroundings imaged by high-resolution tomography, *Geophys. J. Int.*, *194*(2), 1203–1215, doi:10.1093/gji/ggt159.
- Kennett, B. L. N., and E. R. Engdahl (1991), Traveltimes for global earthquake location and phase identification, *Geophys. J. Int.*, *105*, 429–465, doi:10.1111/j.1365-246X.1991.tb06724.x.
- Kissling, E., S. M. Schmid, R. Lippitsch, J. Ansorge, and B. Fügenschuh (2006), Lithosphere structure and tectonic evolution of the Alpine arc: New evidence from high-resolution teleseismic tomography, in *European Lithosphere Dynamics, Memoirs*, vol. 32, edited by D. G. Gee and R. A. Stephenson, pp. 129–145, Geol. Soc., London, doi:10.1144/GSL.MEM.2006.032.01.08.
- Kouřalov, I., M. K. Kaban, M. Tesau, and S. Cloetingh (2009), P- and S- velocity anomalies in the upper mantle beneath Europe from tomographic inversion of ISC data, *Geophys. J. Int.*, *179*, 345–366, doi:10.1111/j.1365-246X.2009.04279.x.
- Linnemann, U., et al. (2008), Precambrian, in *The Geology of Central Europe*, edited by T. McCann, pp. 21–101, Geol. Soc., London, U. K.
- Lippitsch, R., E. Kissling, and J. Ansorge (2003), Upper mantle structure beneath the Alpine orogen from high-resolution teleseismic tomography, *J. Geophys. Res.*, *108*(B8), 2376, doi:10.1029/2002JB002016.
- Matte, P. (1986), Tectonics and plate-tectonics model for the variscan belt of Europe, *Tectonophysics*, *126*, 329–374, doi:10.1016/0040-1951(86)90237-4.
- Menke, W. (1984), *Geophysical Data Analysis: Discrete Inverse Theory*, Academic, Orlando, Fla.
- Mitterbauer, U., M. Behm, E. Brückl, R. Lippitsch, A. Guterch, G. R. Keller, E. Kozlovskaya, E. M. Rumpfhuber, and F. Šumanovac (2011), Shape and origin of the East-Alpine slab constrained by the ALPASS teleseismic model, *Tectonophysics*, *510*, 195–206, doi:10.1016/j.tecto.2011.07.001.
- Petek, A., C. D. Reuther, and R. Schunk (2011), Neotectonic evolution of the Cheb Basin (Northwestern Bohemia, Czech Republic) and its implications for the late Pliocene to recent crustal deformation in the western part of the Eger Rift, *Z. Geol. Wiss.*, *39*(5/6), 335–365.
- Piromallo, C., and A. Morelli (2003), P wave tomography of the mantle under the Alpine-Mediterranean area, *J. Geophys. Res.*, *108*(B2), 2065, doi:10.1029/2002JB001757.
- Plomerová, J., and V. Babuška (2010), Long memory of mantle lithosphere fabric—European LAB constrained from seismic anisotropy, *Lithos*, *120*, 131–143, doi:10.1016/j.lithos.2010.01.008.
- Plomerová, J., V. Babuška, J. Šílený, and J. Horálek (1998), Seismic anisotropy and velocity variations in the mantle beneath the Saxothuringicum-Moldanubicum contact in central Europe, *Pure Appl. Geophys.*, *151*, 365–394, doi:10.1007/s000240050118.
- Plomerová, J., U. Achauer, V. Babuška, M. Granet, and Bohemia Working Group (2003), BOHEMA 2001–2003—Passive seismic experiment to study lithosphere-asthenosphere system in the western part of the Bohemian Massif, *Stud. Geophys. Geod.*, *47*, 691–701, doi:10.1023/A:1024784223048.
- Plomerová, J., L. Vecsey, V. Babuška, M. Granet, and U. Achauer (2005), Passive seismic experiment MOSAIC – a pilot study of mantle lithosphere anisotropy of the Bohemian Massif, *Stud. Geophys. Geod.*, *49*, 541–560, doi:10.1007/s11200-005-0026-0.
- Plomerová, J., U. Achauer, V. Babuška, and L. Vecsey (2007), Upper mantle beneath the Eger Rift (Central Europe): Plume or asthenosphere upwelling?, *Geophys. J. Int.*, *169*(2), 675–682, doi:10.1111/j.1365-246X.2007.03361.x.
- Plomerová, J., L. Vecsey, and V. Babuška (2012), Mapping seismic anisotropy of the lithospheric mantle beneath the northern and eastern Bohemian Massif (central Europe), *Tectonophysics*, *564-565*, 38–53, doi:10.1016/j.tecto.2011.08.
- Ritter, J. R. R., M. Jordan, U. R. Christensen, and U. Achauer (2001), A mantle plume below the Eifel volcanic fields, Germany, *Earth Planet. Sci. Lett.*, *186*, 7–14, doi:10.1016/S0012-821X(01)00226-6.
- Sandoval, S., E. Kissling, J. Ansorge, and SVEKALAKO Seismic Tomography Working Group (2004), High-resolution body wave tomography beneath the SVEKALAPKO array—II. Anomalous upper mantle structure beneath the central Baltic Shield, *Geophys. J. Int.*, *157*, 200–214, doi:10.1111/j.1365-246X.2004.02131.x.
- Shomali, Z. H., R. G. Roberts, L. B. Pedersen, and the TOR Working Group (2006), Lithospheric structure of the Tornquist Zone resolved by nonlinear P and S teleseismic tomography along the TOR array, *Tectonophysics*, *416*, 133–149, doi:10.1016/j.tecto.2005.11.019.
- Stammler, K. (1993), Seismic Handler—Programable multichannel data handler for interactive and automatic processing of seismological analyses, *Comput. Geosci.*, *19*, 135–140, doi:10.1016/0098-3004(93)90110-Q.
- Steck, L. K., W. A. Prothero (1991), A 3-D ray-tracer for teleseismic body-wave arrival-times, *Bull. Seismol. Soc. Am.*, *81*, 1332–1339.
- Ulrych, J., V. Cajz, E. Pivec, J. K. Novák, and Č. Nekovář (2000), Cenozoic intraplate alkaline volcanism of western Bohemia, *Stud. Geophys. Geod.*, *44*, 346–351, doi:10.1023/A:1022131413783.
- Walker, K. T., G. H. R. Bokelmann, S. L. Klemperer, and G. Bock (2005), Shear-wave splitting around the Eifel hotspot: Evidence for a mantle upwelling, *Geophys. J. Int.*, *163*, 962–980, doi:10.1111/j.1365-246X.2005.02636.x.
- Weidle, C., S. Widiyantoro, and CALIXTO Working Group (2005), Improving depth resolution of teleseismic tomography by simultaneous inversion of teleseismic and global P-wave traveltime data—Application to the Vrancea region in Southeastern Europe, *Geophys. J. Int.*, *162*, 811–823, doi:10.1111/j.1365-246X.2005.02649.x.
- Wilde-Piörko, M., et al. (2008), PASSEQ 2006–2008: Passive seismic experiment in Trans-European Suture Zone, *Stud. Geophys. Geod.*, *52*, 439–448, doi:10.1007/s11200-008-0030-2.
- Wilson, M., and H. Downes (2006), Tertiary-Quaternary intra-plate magmatism in Europe and its relationship to mantle dynamics, in *European lithosphere dynamics, Memoirs*, vol. 32, edited by D. G. Gee and R. A. Stephenson, pp. 147–166, Geol. Soc., London, doi:10.1144/GSL.MEM.2006.032.01.09.
- Wortel, M. J. R., and W. Spakman (2000), Subduction and slab detachment in the Mediterranean-Carpathian region, *Science*, *290*, 910–917.
- Ziegler, P. A. (1992), European Cenozoic rift system, *Tectonophysics*, *208*, 91–111, doi:10.1016/0040-1951(92)90338-7.
- Ziegler, P. A., and P. Dezes (2006), Crustal evolution of Western and Central Europe, in *European Lithosphere Dynamics, Memoirs*, vol. 32, edited by D. G. Gee and R. A. Stephenson, pp. 43–56, Geol. Soc., London, doi:10.1144/GSL.MEM.2006.032.01.03.
- Ziegler, P. A., M. E. Schumacher, P. Dezes, J. D. Van Wees, and S. Cloetingh (2006), Post-Variscan evolution of the lithosphere in the area of the European Cenozoic Rift System, in *European Lithosphere Dynamics, Memoirs*, vol. 32, edited by D. G. Gee and R. A. Stephenson, pp. 97–112, Geol. Soc., London, doi:10.1144/GSL.MEM.2006.032.01.06.